

1 Characterization of Errors in Satellite-based HCHO/NO₂ 2 Tropospheric Column Ratios with Respect to Chemistry, Column to 3 PBL Translation, Spatial Representation, and Retrieval 4 Uncertainties

5
6
7 Amir H. Souri^{1,2,3*}, Matthew S. Johnson⁴, Glenn M. Wolfe², James H. Crawford⁵, Alan Fried⁶,
8 Armin Wisthaler^{7,8}, William H. Brune⁹, Donald R. Blake¹⁰, Andrew J. Weinheimer¹¹, Tijn
9 Verhoelst¹², Steven Compornolle¹², Gaia Pinaridi¹², Corinne Vigouroux¹², Bavo Langerock¹²,
10 Sungyeon Choi^{2,13}, Lok Lamsal^{2,14}, Lei Zhu^{15,16}, Shuai Sun^{15,16}, Ronald C. Cohen^{17,18}, Kyung-Eun
11 Min¹⁹, Changmin Cho¹⁹, Sajeev Philip²⁰, Xiong Liu¹, and Kelly Chance¹

12
13 ¹Atomic and Molecular Physics (AMP) Division, Center for Astrophysics | Harvard & Smithsonian,
14 Cambridge, MA, USA

15 ²Atmospheric Chemistry and Dynamics Laboratory, NASA Goddard Space Flight Center, Greenbelt,
16 MD, USA

17 ³GESTAR II, Morgan State University, Baltimore, MD, USA

18 ⁴Earth Science Division, NASA Ames Research Center, Moffett Field, CA, USA

19 ⁵NASA Langley Research Center, Hampton, VA, USA

20 ⁶Institute of Arctic & Alpine Research, University of Colorado, Boulder, CO, USA

21 ⁷Institute for Ion Physics and Applied Physics, University of Innsbruck, Technikerstrasse 25, 6020
22 Innsbruck, Austria

23 ⁸Department of Chemistry, University of Oslo, P.O. box 1033, Blindern, 0315 Oslo, Norway

24 ⁹Department of Meteorology and Atmospheric Science, Pennsylvania State University, University Park,
25 PA, USA

26 ¹⁰Department of Chemistry, University of California, Irvine, CA, USA

27 ¹¹National Center for Atmospheric Research, Boulder, CO, USA

28 ¹²Royal Belgian Institute for Space Aeronomy (BIRA-IASB), Ringlaan 3, 1180 Uccle, Belgium

29 ¹³Science Systems and Applications, Inc., Lanham, MD 20706, USA

30 ¹⁴Universities Space Research Association, Columbia, MD 21046, USA

31 ¹⁵School of Environmental Science and Engineering, Southern University of Science and Technology,
32 Shenzhen, Guangdong, China

33 ¹⁶Guangdong Provincial Observation and Research Station for Coastal Atmosphere and Climate of the
34 Greater Bay Area, Shenzhen, Guangdong, China

35 ¹⁷Department of Earth and Planetary Science, University of California Berkeley, Berkeley, CA 94720, USA

36 ¹⁸Department of Chemistry, University of California Berkeley, Berkeley, CA 94720, USA

37 ¹⁹School of Earth Sciences and Environmental Engineering, Gwangju Institute of Science and Technology,
38 Gwangju, South Korea

39 ²⁰Centre for Atmospheric Sciences, Indian Institute of Technology Delhi, New Delhi, India

40
41 * Corresponding Author: a.souri@nasa.gov (amir.souri@morgan.edu)

42 43 **Abstract.**

44 The availability of formaldehyde (HCHO) (a proxy for volatile organic compound
45 reactivity) and nitrogen dioxide (NO₂) (a proxy for nitrogen oxides) tropospheric columns from
46 Ultraviolet-Visible (UV-Vis) satellites has motivated many to use their ratios to gain some insights
47 into the near-surface ozone sensitivity. Strong emphasis has been placed on the challenges that

48 come with transforming what is being observed in the tropospheric column to what is actually in
49 the planetary boundary layer (PBL) and near the surface; however, little attention has been paid to
50 other sources of error such as chemistry, spatial representation, and retrieval uncertainties. Here
51 we leverage a wide spectrum of tools and data to quantify those errors carefully.

52 Concerning the chemistry error, a well-characterized box model constrained by more than
53 500 hours of aircraft data from NASA's air quality campaigns is used to simulate the ratio of the
54 chemical loss of HO₂+RO₂ (LRO_x) to the chemical loss of NO_x (LNO_x). Subsequently, we
55 challenge the predictive power of HCHO/NO₂ ratios (FNRs), which are commonly applied in
56 current research, at detecting the underlying ozone regimes by comparing them to LRO_x/LNO_x.
57 FNRs show a strongly linear (R²=0.94) relationship to LRO_x/LNO_x, but only in the logarithmic
58 scale. Following the baseline (i.e., ln(LRO_x/LNO_x) = -1.0±0.2) with the model and mechanism
59 (CB06, r2) used for segregating NO_x-sensitive from VOC-sensitive regimes, we observe a broad
60 range of FNR thresholds ranging from 1 to 4. The transitioning ratios strictly follow a Gaussian
61 distribution with a mean and standard deviation of 1.8 and 0.4, respectively. This implies that FNR
62 has an inherent 20% standard error (1-sigma) resulting from not accurately describing the RO_x-
63 HO_x cycle. We calculate high ozone production rates (PO₃) dominated by large HCHO×NO₂
64 concentration levels, a new proxy for the abundance of ozone precursors. The relationship between
65 PO₃ and HCHO×NO₂ becomes more pronounced when moving towards NO_x-sensitive regions
66 due to non-linear chemistry; our results indicate that there is fruitful information in the
67 HCHO×NO₂ metric that has not been utilized in ozone studies. The vast amount of vertical
68 information on HCHO and NO₂ concentration from the air quality campaigns enables us to
69 parameterize the vertical shapes of FNRs using a second-order rational function permitting an
70 analytical solution for an altitude adjustment factor to partition the tropospheric columns to the
71 PBL region. We propose a mathematical solution to the spatial representation error based on
72 modeling isotropic semivariograms. Based on summertime averaged data, Ozone Monitoring
73 Instrument (OMI) loses 12% of spatial information at its native resolution with respect to a high-
74 resolution sensor like TROPospheric Monitoring Instrument (TROPOMI) (>5.5×3.5 km²). A
75 pixel with a grid size of 216 km² fails at capturing ~65% of the spatial information in FNRs at a
76 50 km length scale comparable to the size of a large urban center (e.g., Los Angeles). We
77 ultimately leverage a large suite of in-situ and ground-based remote sensing measurements to draw
78 the error distributions of daily TROPOMI and OMI tropospheric NO₂ and HCHO columns. At a
79 68% confidence interval (1 sigma), errors pertaining to daily TROPOMI observations, either
80 HCHO or tropospheric NO₂ columns, should be above 1.2-1.5×10¹⁶ molec.cm⁻² to attain 20-30%
81 standard error in the ratio. This level of error is almost non-achievable with OMI, given its large
82 error in HCHO.

83 The satellite column retrieval error is the largest contributor to the total error (40-90%) in
84 the FNRs. Due to a stronger signal in cities, the total relative error (<50%) tends to be mild,
85 whereas areas with low vegetation and anthropogenic sources (e.g., Rocky Mountains) are
86 markedly uncertain (>100%). Our study suggests that continuing development in the retrieval
87 algorithm and sensor design and calibration is essential to be able to advance the application of
88 FNRs beyond a qualitative metric.

89 **1. Introduction**

90 Accurately representing the near-surface ozone (O₃) sensitivity to its two major precursors,
91 nitrogen oxides (NO_x) and volatile organic compounds (VOCs), is an imperative step in
92 understanding non-linear chemistry associated with ozone production rates in the atmosphere.
93 While it is often tempting to characterize an airshed as NO_x or VOC-sensitive, both conditions are

94 expected as VOC-sensitive (ozone production rates sensitive to VOC) conditions near NOx
95 sources transition to NOx-sensitive (ozone production rates sensitive to NOx) conditions
96 downwind as NOx dilutes. Thus, reducing the footprint of ozone production can mostly be
97 achieved through NOx reductions. VOCs are key to determining both the location and peak in
98 ozone production, which varies nonlinearly to the NOx abundance. Thus, knowledge of the relative
99 levels of NOx and VOCs informs the trajectory of ozone production and expectations of where
100 peak ozone will occur as emissions change. While a large number of surface stations regularly
101 monitor the near-surface ambient nitrogen dioxide (NO₂) concentrations, the measurements of
102 several VOCs with different reactivity rates with respect to hydroxyl (OH) are not routinely
103 available. As such, our knowledge of where and when ozone production rates are elevated, and
104 their quantitative dependence on a long list of ozone precursors, is fairly limited, except for
105 observationally-rich air quality campaigns. This limitation has prompted several studies, such as
106 Sillman et al. (1990), Tonnesen and Dennis (2000a,b), and Sillman and He (2002), to investigate
107 if the ratio of certain measurable compounds can diagnose ozone regimes meaning if the ozone
108 production rate is sensitive to NOx (i.e., NOx-sensitive) or VOC (i.e., VOC-sensitive). Sillman
109 and He (2002) suggested that H₂O₂/HNO₃ was a robust, measurable ozone indicator as this ratio
110 could well describe the chemical loss of HO₂+RO₂ (LROx) to the chemical loss of NOx (LNOx)
111 controlling the O₃-NOx-VOC chemistry (Kleinman et al., 2001). Nonetheless, both H₂O₂ and
112 HNO₃ measurements are limited to a few spatially-sparse air quality campaigns.

113 Formaldehyde (HCHO) is an oxidation product of VOCs, and its relatively short lifetime
114 (~1-9 hr) makes the location of its primary and secondary sources rather identifiable (Seinfeld and
115 Pandis, 2006; Fried et al., 2020). Fortunately, monitoring HCHO abundance in the atmosphere has
116 been a key goal of many Ultraviolet-Visible (UV-Vis) viewing satellites for decades (Chance et
117 al., 1991; Chance et al., 1997; Chance et al., 2000; González Abad et al., 2015; De Smedt et al.,
118 2008, 2012, 2015, 2018, 2021) with reasonable spatial coverage. Additionally, the strong
119 absorption of NO₂ in the UV-Vis range has permitted measurements of NO₂ columns from space
120 (Martin et al., 2002; Boersma et al., 2004, 2007, 2018).

121 Advancements in satellite remote-sensing of these two key compounds have encouraged
122 many studies to elucidate if the ratio of HCHO/NO₂ (hereafter FNR) could be a robust ozone
123 indicator (Tonnesen and Dennis, 2000b; Martin et al., 2004; Duncan et al., 2010). Most studies
124 using the satellite-based FNR columns attempted to provide a qualitative view of the underlying
125 chemical regimes (e.g., Choi et al., 2012; Choi and Souri, 2015a,b; Jin and Holloway, 2015; Souri
126 et al., 2017; Jeon et al., 2018; Lee et al., 2021). Relatively few studies (Duncan et al., 2010; Jin et
127 al., 2017; Schroeder et al., 2017; Souri et al., 2020) have carefully tried to provide a quantitative
128 view of the usefulness of the ratio. For the most part, the inhomogeneous vertical distribution of
129 FNR in columns has been emphasized. Jin et al. (2017) and Schroeder et al. (2017) showed that
130 differing vertical shapes of HCHO and NO₂ can cause the vertical shape of FNR not to be
131 consistent throughout the troposphere leading to a variable relationship between what is being
132 observed from the satellite and what is actually occurring in the lower atmosphere. Jin et al. (2017)
133 calculated an adjustment factor to translate the column to the surface using a relatively coarse
134 global chemical transport model. The adjustment factor showed a clear seasonal cycle stemming
135 from spatial and temporal variability associated with the vertical sources and sinks of HCHO and
136 NO₂, in addition to the atmospheric dynamics. In a more data-driven approach, Schroeder et al.
137 (2017) found that the detailed differences in the boundary layer vertical distributions of HCHO
138 and NO₂ lead to a wide range of ambiguous ratios. Additionally, ratios were shown to shift on high
139 ozone days, raising questions regarding the value of satellite averages over longer timescales. Our

140 research aims to put together an integrated and data-driven mathematical formula to translate the
141 tropospheric column to the planetary boundary layer (PBL), exploiting the abundant aircraft
142 measurements available during ozone seasons.

143 Using observationally-constrained box models, Souri et al. (2020) demonstrated that there
144 was a fundamentally inherent uncertainty related to the ratio originating from the chemical
145 dependency of HCHO on NO_x (Wolfe et al., 2016). In VOC-rich (poor) environments, the
146 transitioning ratios from NO_x-sensitive to VOC-sensitive occurred in larger (smaller) values than
147 the conventional thresholds defined in Duncan et al. (2010) due to an increased (dampened) HCHO
148 production induced by NO_x. To account for the chemical feedback and to prevent a wide range of
149 thresholds on segregating NO_x-sensitive from VOC-sensitive regions, Souri et al. (2020)
150 suggested using a first-order polynomial matched to the ridgeline in P(O₃) isopleths. Their study
151 illuminated the fact that the ratio suffers from an inherent chemical complication. However, Souri
152 et al. (2020) did not quantify the error, and their work was limited to a subset of atmospheric
153 conditions. To challenge the predictive power of FNR from a chemistry perspective, we will take
154 advantage of a large suite of datasets to make maximum use of varying meteorological and
155 chemical conditions.

156 Not only are satellite-based column measurements unable to resolve the vertical
157 information of chemical species in the tropospheric column, but they are also unable to resolve the
158 horizontal spatial variability due to their spatial footprint. The larger the footprint is, the more
159 horizontal information is blurred out. For instance, Souri et al. (2020) observed a substantial spatial
160 variance (information) in FNR columns at the spatial resolution of 250×250 m² observed by an
161 airborne sensor over Seoul, South Korea. It is intuitively clear that a coarse-resolution sensor
162 would lose a large degree of spatial variance (information). This error, known as the spatial
163 representation error, has not been studied with respect to FNR. We will leverage what we have
164 learned from Souri et al. (2022), which modeled the spatial heterogeneity in discrete data using
165 geostatistics, to quantify the spatial representation error in the ratio over an urban environment.

166 A longstanding challenge is to have a reliable estimate of the satellite retrieval errors of
167 tropospheric column NO₂ and HCHO. Significant efforts have been made recently to assemble,
168 analyze, and estimate the retrieval errors for two key satellite sensors, TROPOspheric Monitoring
169 Instrument (TROPOMI) and Ozone Monitoring Instrument (OMI), using various in-situ
170 measurements (Verhoelst et al., 2021; Vigouroux et al., 2020, Choi et al., 2020; Laughner et al.,
171 2019; Zhu et al., 2020). This study will exploit paired comparisons from some of these new studies
172 to propagate individual uncertainties in HCHO and NO₂ to the FNR errors.

173 The overarching science goal of this study is to address the fact that the accurate diagnosis
174 of surface O₃ photochemical regimes is impeded by numerous uncertainty components, which will
175 be addressed in the current paper, and can be classified into four major categories: i) inherent
176 uncertainties associated with the approach of FNRs to diagnose local O₃ production and sensitivity
177 regimes, ii) translation of tropospheric column satellite retrievals to represent PBL- or surface-
178 level chemistry, iii) spatial representativity of ground pixels of satellite sensors, and iv)
179 uncertainties associated with satellite-retrieved column-integrated concentrations of HCHO and
180 NO₂. We will address all of these sources of uncertainty using a broad spectrum of data and tools.

181 Our paper is organized into the following sections. Section 2 describes the chemical box
182 model setup and data applied. Sections 3.1 to 3.4 deal with the chemistry aspects of FNRs and
183 show the results from a box model. Section 3.5 introduces a data-driven framework to transform
184 the FNR tropospheric columns to the PBL region. Section 3.6 offers a new way to quantify the
185 spatial representation error in satellites. Section 3.7 deals with the satellite error characterization

186 and its impacts on the ratio. Section 3.8 summarizes the fractional contribution of each error to the
187 combined error. Finally, Section 4 provides a summary and conclusions of the study.

188 **2. Photochemical Box Modeling and Aircraft Data Used**

189 To quantify the uncertainty of FNR from a chemistry perspective and to obtain several
190 imperative parameters, including the calculated ozone production rates and the loss of NO_x (LNO_x)
191 and RO_x (LRO_x), we utilize the Framework for 0-D Atmospheric Modeling (FOAM) v4 (Wolfe et
192 al., 2016). We adopt the Carbon Bond 6 (CB06, r2) chemical mechanism, and heterogenous
193 chemistry is not considered in our simulations. The model is initialized with the measurements of
194 several compounds, many of which constrain the model by being held constant for each timestep
195 (see Table 1).

196 Figure 1 shows the map of data points from Deriving Information on Surface Conditions
197 from Column and Vertically Resolved Observations Relevant to Air Quality (DISCOVER-AQ)
198 Baltimore-Washington (2011), DISCOVER-AQ Houston-Texas (2013), DISCOVER-AQ
199 Colorado (2014), and Korea United States Air Quality Study (KORUS-AQ) (2016).
200 Meteorological inputs come from the observed pressure, temperature, and relative humidity. The
201 measurements of photolysis rates are not available for all photolysis reactions; therefore, our initial
202 guess of those rates comes from a look-up-table populated by the National Center for Atmospheric
203 Research (NCAR) Tropospheric Ultraviolet And Visible (TUV) model calculations. These values
204 are a function of solar zenith angle, total ozone column density, surface albedo, and altitude. We
205 set the total ozone column and the surface albedo to fixed numbers of 325 (Dobson) DU and 0.15,
206 respectively. The initial guess is then corrected by applying the ratio of observed photolysis rates
207 of $\text{NO}_2+\text{h}\nu$ ($j\text{NO}_2$) and/or $\text{O}_3+\text{h}\nu$ ($j\text{O}^1\text{D}$) to the calculated ones to all j -values (i.e., wavelength-
208 independent). If both observations of $j\text{NO}_2$ and $j\text{O}^1\text{D}$ are available, the correction factor is
209 averaged. The KORUS-AQ campaign is the only one that provides $j\text{O}^1\text{D}$ measurements; therefore,
210 the use of the wavelength-independent correction factor based on the ratio of observed to
211 calculated $j\text{NO}_2$ values for all j -value is a potential source of error in the model especially when
212 aerosols are present. The model calculations are based on the observations merged to a temporal
213 resolution varying from 10 to 15 seconds. Each calculation was run for five consecutive days with
214 an integration time of 1 hour to approach diel steady state. We test the number of solar cycles
215 against ten days on the KORUS-AQ setup and observe no noticeable difference in simulated OH
216 and HCHO (Figure S1), indicating that five solar cycles suffice. Some secondarily-formed species
217 must be unconstrained for the purpose of model validation. Therefore, the concentrations of several
218 secondarily-formed compounds, such as HCHO and PAN, are unconstrained. Nitric oxide (NO)
219 and NO_2 are also allowed to cycle while their sum (i.e., NO_x) is constrained. Because the model
220 does not consider various physical loss pathways, including deposition and transport, which vary
221 by time and space, we oversimplify their physical loss through a first-order dilution rate set to
222 $1/86400-1/43200 \text{ s}^{-1}$ (i.e., 24- or 12-hr lifetime), which in turn prevents relatively long-lived
223 species from accumulating over time. Our decision on unconstraining HCHO, a pivotal compound
224 impacting the simulation of HO_x, may introduce some systematic biases in the simulation of
225 radicals determining ozone chemistry (Schroeder et al., 2020). Therefore, to mitigate the potential
226 bias in HCHO, we set the dilution factor to maintain the campaign-averaged bias in the simulated
227 HCHO with respect to observations of less than 5%. However, it is essential to recognize that
228 HCHO can fluctuate freely for each point measurement because the dilution constraint is set to a
229 fixed value for an individual campaign. Each time tag is independently simulated, meaning we do
230 not initialize the next run using the simulated values from the previous one; this in turn, permits
231 parallel computation. Regarding the KORUS-AQ campaign where HO_x observations were

232 available, we only ran the model for data points with HO_x measurements. Similar to Souri et al.
 233 (2020), we filled gaps in VOC observations with a bilinear interpolation method with no
 234 extrapolation allowed. In complex polluted atmospheric conditions such as that over Seoul, South
 235 Korea, Souri et al. (2020) observed that this simple treatment yielded comparable results with
 236 respect to the NASA LaRC model (Schroeder et al. 2020), which incorporated a more
 237 comprehensive data harmonization. Table 1 lists the major configuration along with the
 238 observations used for the box model.

239 Several parameters are calculated based on the box model outputs. LRO_x is defined through
 240 the sum of primarily radical-radical reactions:

$$LRO_x = k_{HO_2+HO_2}[HO_2]^2 + \sum k_{RO_{2i}+HO_2}[RO_{2i}][HO_2] + \sum k_{RO_{2i}+RO_{2i}}[RO_{2i}]^2 \quad (1)$$

241 where k is the reaction rate constant. LNO_x mainly occurs via the NO₂+OH reaction:

$$LNO_x = k_{OH+NO_2+M}[OH][NO_2][M] \quad (2)$$

242 where M is a third body. We calculate P(O₃) by subtracting the ozone loss pathways dictated by
 243 HO_x (HO+HO₂), NO₂+OH, O₃ photolysis, ozonolysis, and the reaction of O(¹D) with water vapor
 244 from the formation pathways through the removal of NO via HO₂ and RO₂:

$$P(O_3) = k_{HO_2+NO}[HO_2][NO] + \sum k_{RO_{2i}+NO}[RO_{2i}][NO] - k_{OH+NO_2+M}[OH][NO_2][M] - P(RONO_2) - k_{HO_2+O_3}[HO_2][O_3] - k_{OH+O_3}[OH][O_3] - k_{O(^1D)+H_2O}[O(^1D)][H_2O] - L(O_3 + alkenes) \quad (3)$$

245 3. Results and Discussion

246 3.1. Box Model Validation

247 There are uncertainties associated with the box model (e.g., Brune et al., 2022; Zhang et
 248 al., 2021; Lee et al., 2021), which can be attributed to: i) the lack of inclusion of physical processes
 249 such as entrainment/detrainment and diffusion, ii) discounting the heterogeneous chemistry, iii)
 250 invalid assumption of the diel steady state in areas close to large emission sources or in
 251 photochemically less active environments (Thornton et al., 2002; Souri et al., 2021), iv) errors in
 252 the chemical mechanism and v) errors in the measurements. These limitations necessitate a
 253 thorough validation of the model using unconstrained observations. While models have been
 254 known for a long time not to be 100% accurate (Box, 1976), it is important to characterize whether
 255 the model can effectively represent reality. For instance, if the simulated HCHO is poorly
 256 correlated with observations and/or displayed large magnitude biases, it will be erroneous to
 257 assume that the sources of HCHO, along with relevant chemical pathways, are appropriate. It is
 258 important to acknowledge that the VOC constraints for these model calculations are incomplete,
 259 especially for the DISCOVER-AQ campaigns, which lacked comprehensive VOC observations.
 260 Nevertheless, we will show that the selected VOCs are sufficient to reproduce a large variance
 261 (>70%) in observed HCHO.

262 We diagnose the performance of the box model by comparing the simulated values of five
 263 compounds to observations: HCHO, NO, NO₂, PAN, hydroperoxyl radical (HO₂), and OH. Figure
 264 2 depicts the scatterplot of the comparisons along with several statistics. HCHO observations are
 265 usually constrained in box models to improve the representation of HO₂ (Schroeder et al., 2017;

266 Souri et al., 2020; Brune et al., 2022); however, this constraint may mask the realistic
267 characterization of the chemical mechanism with respect to the treatment of VOCs. Additionally,
268 it is important to know if the sources of HCHO are adequate. Therefore, we detach the model from
269 this constraint to perform a more fair and stringent validation.

270 Concerning HCHO, our model does have considerable skill at reproducing the variability
271 of observed HCHO ($R^2=0.73$). To evaluate if this agreement is accidentally caused by the choice
272 of the dilution factor and to identify if our VOC treatment is inferior compared to the one adopted
273 in the NASA LaRC (Schroeder et al., 2021), we conducted three sets of sensitivity tests for the
274 KORUS-AQ campaign, including ones with and without considering a dilution factor and another
275 one without HNO_3 and H_2O_2 constraints (Figure S2). The lack of consideration of a dilution factor
276 results in no difference in the variance in HCHO captured by our model ($R^2=0.81$). Our model
277 without the dilution factor is still skillful at replicating the magnitude of HCHO with less than 12%
278 bias. This is why the optimal dilution factor for each campaign is within 12 hr to 24 hr, which is
279 not different from other box modeling studies (e.g., Brune et al., 2022; Miller and Brune, 2022).
280 We observe no difference in the simulated HCHO when HNO_3 and H_2O_2 values are not
281 constrained. The unconstrained NASA LaRC setup oversampled at 10-sec frequency captures 86%
282 variance in the measurements, only slightly (6%) outperforming our result. However, the
283 unconstrained NASA LaRC setup greatly underestimates the magnitude of HCHO compared to
284 our model results.

285 The model performs well with regard to the simulation of NO ($R^2=0.89$) and NO_2 ($R^2=0.99$)
286 in the logarithmic scale. Immediately evident is the underestimation of NO in highly polluted
287 regions, contrary to an overestimation in clean ones. This discrepancy leads to an underestimation
288 (overestimation) of NO/ NO_2 in polluted (clean) regions. The primary drivers of NO/ NO_2 are j NO_2
289 and O_3 , both of which are constrained in the model. What can essentially deviate the partitioning
290 between NO and NO_2 from that of observations in polluted areas is the assumption of the diel
291 steady state, which is rarely strictly valid where measurements are close to large emitters. The
292 overestimation of NO in low NO_x areas is often blamed on the lack of chemical sink pathways of
293 NO in chemical mechanisms (e.g., Newland et al., 2021). The relatively reasonable performance
294 of PAN ($R^2=0.63$) is possibly due to constraining some of the oxygenated VOCs, such as
295 acetaldehyde. Xu et al. (2021) observed a strong dependency of PAN concentrations on NO/ NO_2
296 ratios. Smaller NO/ NO_2 ratios are usually associated with larger PAN mixing ratios because NO
297 can effectively remove peroxyacetyl radicals. We observe an overestimated PAN (0.27 ppbv),
298 possibly due to an underestimation of NO/ NO_2 . Moreover, we should not rule out the impact of
299 the first-order dilution factor, which was only empirically set in this study. For instance, if we
300 ignore the dilution process for the KORUS-AQ campaign, the bias of the model in terms of PAN
301 will increase by 33% resulting in poor performance ($R^2=0.40$) (Figure S3). We notice that this
302 poor performance primarily occurs for high altitude measurements where PAN is thermally stable
303 (Figure S4); therefore, this does not impact the majority of rapid atmospheric chemistry occurring
304 in the lower troposphere, such as the formation of HCHO. Schroeder et al. (2020) found that proper
305 simulation of PAN in the polluted PBL during KORUS-AQ required a first-order loss rate based
306 on thermal decomposition at the average PBL temperature, which was more realistic than the
307 widely varying local PAN lifetimes associated with temperature gradients between the surface and
308 the top of the PBL. This solution is computationally equivalent to the dilution rate used in this
309 study.

310 KORUS-AQ was the only field campaign providing OH and HO_2 measurements.
311 Concerning HO_2 , former studies such as Schroeder et al. (2017), Souri et al. (2020), and Brune et

312 al. (2022) managed to reproduce HO₂ mixing ratios with R² ranging from 0.6 to 0.7. The
313 performance of our model (R²=0.66) is similar to these past studies, with nearly negligible biases
314 (<1%). One may argue that the absence of the HO₂ uptake by aerosols is contributing to some of
315 the discrepancies we observe in the HO₂ comparison. Brune et al. (2022) provided compelling
316 evidence showing that considering the HO₂ uptake made their results significantly inconsistent
317 with the observations suggesting that the HO₂ uptake might have been inconsequential during the
318 campaign. Our model manages to reproduce 64% of the variance of observed OH outperforming
319 the simulations presented in Souri et al. (2020) and Brune et al. (2022) by >10%. The slope (=
320 1.03) is not too far from the identity line, indicating that our box model systematically
321 overestimates OH by 0.62 10⁶ cm⁻³. This may be attributed to a missing OH sink in the mechanism
322 or the lack of inclusion of some VOCs. A sensitivity test involving removing the first-order
323 dilution process demonstrates that the simulation of HO_x is rather insensitive to this parameter
324 (Figure S5). In general, the model performance is consistent, or outperforms, results from recent
325 box modeling studies, indicating that it is at least roughly representative of the real-world ozone
326 chemistry and sensitivity regimes.

327 **3.2. Can HCHO/NO₂ ratios fully describe the HO_x-RO_x cycle?**

328 Kleinman et al. (2001) demonstrated that LRO_x/LNO_x is the most robust ozone regime
329 indicator. Thus, the predictive power of FNR at detecting the underlying chemical conditions can
330 be challenged by comparing FNR to LRO_x/LNO_x. Ideally, if they show a strong degree of
331 correspondence (i.e., R²=1.0), we can confidently say that FNR can realistically portray the
332 chemical regimes. Any divergence of these two quantities indicates the inadequacy of the FNR
333 indicator. Souri et al. (2020) observed a strong linear relationship between the logarithmic
334 transformed FNR and those of LRO_x/LNO_x. Our analysis in this study will be based on the
335 simulated values to ensure that the relationship is coherent based on a realization from the well-
336 characterized box model. As pointed out by Schroeder et al. (2017) and Souri et al. (2020), a
337 natural logarithm of LRO_x/LNO_x roughly equal to -1.0 (i.e., LRO_x/LNO_x = 0.35-0.37)
338 perceptibly separates VOC-sensitive from NO_x-sensitive regimes, which would make this
339 threshold the baseline of our analysis.

340 Figure 3 demonstrates the log-log relationship of LRO_x/LNO_x and FNR, and P(O₃), from
341 all four air quality campaigns. The log-log relationships from each individual campaign are shown
342 in Figure S6-S9. We overlay the LRO_x/LNO_x baseline threshold along with two commonly used
343 thresholds for FNR suggested by Duncan et al. (2010); they defined the VOC-sensitive regimes if
344 FNR<1 and the NO_x-sensitive ones if FNR>2. Any region undergoing a value between these
345 thresholds is unlabeled and considered to be in a transitional regime. The size of each data point
346 is proportional to the HCHO×NO₂ concentration magnitude. One striking finding from this plot is
347 that there is indeed a strong linear relationship between the logarithmic-transformed LRO_x/LNO_x
348 and FNR (R²=0.91). A strong linear relationship between the two quantities in the log-log scale
349 indicates a power law dependence (i.e., y=ax^b). A strong power law dependency means that these
350 two quantities have a poor correlation at their low and high values. This is mainly caused by the
351 fact that HCHO does not fully describe VOC reactivity rates in environments with high and low
352 VOC concentrations (Souri et al., 2020). The question is, what range of FNR will fall in
353 ln(LRO_x/LNO_x) = -1.0±0.2? Following the baseline, the transitioning ratios follow a normal
354 distribution with a mean of 1.8, a standard deviation of 0.4, and a range from 1 to 4 (Figure S10).
355 We define the chemical error in the application of FNR to separate the chemical regimes as the
356 relative error standard deviation (i.e., σ/μ) of the transitioning ratios leading to ~ 20%. These
357 numbers are based on a single model realization and can change if a different mechanism is used;

358 nonetheless, the model has considerable skill at reproducing many different unconstrained
359 compounds, especially OH, suggesting that it is a rather reliable realization. Comparing the
360 transitioning FNRs to the NO₂ concentrations suggests no correlation ($r=0.02$), whereas there is a
361 linear correlation between the transitioning ratios and the HCHO concentrations ($r=0.56$). This
362 tendency reinforces the study of Souri et al. (2020), who, primarily due to the HCHO-NO₂
363 feedback, observed a larger FNR threshold in VOC-rich environments to be able to detect the
364 chemical regimes.

365 **3.3. Large PO₃ rates occur in regions with large HCHO×NO₂ concentrations when** 366 **moving toward NO_x-sensitive regions**

367 A striking and perhaps intuitive tendency observed from Figure 3 is that large PO₃ rates
368 are mostly tied to higher HCHO×NO₂. But this relationship gradually weakens as we move
369 towards VOC-sensitive regions (smaller LRO_x/LNO_x ratios). This is a textbook example of non-
370 linear ozone chemistry. In VOC-sensitive areas, PO₃ can be strongly inhibited by NO₂+OH and
371 the formation of organic nitrates despite the abundance of the precursors. In the application of
372 remote-sensing of ozone precursors, the greatest unused metric describing the mass of the ozone
373 precursors is HCHO×NO₂. However, this metric should only be used in conjunction with FNR. To
374 demonstrate this, based on what the baseline (LRO_x/LNO_x) suggests against thresholds on FNRs
375 defined by Duncan et al. (2010), we group the data into four regions: NO_x-sensitive – NO_x-
376 sensitive, NO_x-sensitive–transitional, VOC-sensitive–transitional, and VOC-sensitive–VOC-
377 sensitive. A different perspective on this categorization is that the transitional regimes are a weaker
378 characterization of the main regime; for instance, NO_x-sensitive–transitional regions are less NO_x-
379 sensitive than NO_x-sensitive – NO_x-sensitive. Subsequently, the cumulative distribution functions
380 (CDFs) of PO₃ and HCHO×NO₂ with respect to the aforementioned groups are calculated, which
381 is shown in Figure 4. Regarding NO_x-sensitive—NO_x-sensitive regions, we see the PO₃ CDF very
382 quickly converging to the probability of 100%, indicating that the distribution of PO₃ is skewed
383 towards very low values. The median of PO₃ for this particular regime (where CDF = 50%) is only
384 0.25 ppbv/hr. This agrees with previous studies such as Martin et al. (2002), Choi et al. (2012), Jin
385 et al. (2017), and Souri et al. (2017), reporting that NO_x-sensitive regimes dominate in pristine
386 areas. The PO₃ CDFs between NO_x-sensitive—transitional and VOC-sensitive—VOC-sensitive
387 are not too distinct, whereas their HCHO×NO₂ CDFs are substantially different. The non-linear
388 ozone chemistry suppresses PO₃ in highly VOC-sensitive areas such that those values are not too
389 different from those in mildly polluted areas (NO_x-sensitive—transitional). Perhaps the most
390 interesting conclusion from this figure is that elevated PO₃ values (median = 4.6 ppbv/hr), a factor
391 of two larger than two previous regimes, are mostly found in VOC-sensitive—transitional. This is
392 primarily due to two causes: i) this particular regime is not strongly inhibited by the nonlinear
393 chemistry, particularly NO₂+OH, and ii) it is associated with abundant precursors evident in the
394 median of HCHO×NO₂ being three times as large of those in NO_x-sensitive—transitional. This
395 tendency illustrates the notion of non-linear chemistry and how this may affect regulations. Simply
396 knowing where the regimes are might not suffice to pinpoint the peak of PO₃, as this analysis
397 suggests that we need to consider both FNR and HCHO×NO₂; both metrics are readily accessible
398 from satellite remote-sensing sensors.

399 **3.4. Can we estimate PO₃ using the information from HCHO/NO₂ and HCHO×NO₂?**

400 It may be advantageous to construct an empirical function fitted to these two quantities and
401 elucidate the maximum variance (information) we can potentially gain to recreate PO₃. After
402 several attempts, we found a bilinear function ($z=a_0+a_1x+a_2y+a_3xy$) to be a good fit without

403 overparameterization. Due to presence of extreme values in both FNR and HCHO×NO₂, we use a
404 weighted least squares method for the curve fitting based on the distance of the fitted curve to the
405 data points (known as bi-squares weighting). The best fit with R² equals to 0.94 and an RMSE of
406 0.60 ppbv/hr is:

$$PO_3 = 0.74 - 0.09x - 0.02y + 0.25xy \quad (4)$$

407 where x and y are FNR (unitless) and HCHO×NO₂ (ppbv²), respectively. The residual of the fit is
408 shown in Figure S11. The gradients of PO₃ with respect to x and y are:

$$\frac{dPO_3}{dx} = 0.25y - 0.09 \quad (5)$$

$$\frac{dPO_3}{dy} = 0.25x - 0.02 \quad (6)$$

409 An apparent observation arises from these equations that is the derivative of PO₃ to each
410 metric depends on the other one underscoring their interconnectedness. For instance, Eq. (6)
411 suggests that larger FNRs (x) result in a larger gradient of PO₃ to the abundance of HCHO×NO₂
412 (y). In very low FNRs, this gradient can become very small, rendering PO₃ insensitive (or in
413 extreme cases, negatively correlated) to HCHO×NO₂. This analysis provides encouraging results
414 about the future application of the satellite-derived HCHO×NO₂; however, the wide class of
415 problems relating to the application of satellite-derived FNR columns, such as satellite errors in
416 columns or the translation between columns to PBL is also present in Eq. (4), even in a more
417 pronounced way due to HCHO×NO₂ and HCHO² (= xy). This new perspective on PO₃ estimation
418 deserves a separate study.

419 3.5. Altitude dependency and its parametrization

420 A lingering concern over the application of satellite-based FNR tropospheric columns is
421 that the vertical distribution of HCHO and NO₂ are integrated into columns; thus, this vertical
422 information is permanently lost. Here, we provide insights into the vertical distribution of FNR
423 within the tropospheric column. This task requires information about the differences between i)
424 the vertical shape of HCHO and that of NO₂ and ii) the vertical shape in the sensitivity of the
425 retrievals to the different altitude layers (described as scattering weights). Ideally, if both
426 compounds show an identically relative shape, the FNR columns will be valid for every air parcel
427 along the vertical path (i.e., a straight line). Previous studies such as Jin et al. (2017) and Schroeder
428 et al. (2017) observed a large degree of vertical inhomogeneity in both HCHO and NO₂
429 concentrations suggesting that this ideal condition cannot be met. We do not always have precise
430 observations of HCHO and NO₂ vertical distributions, but we can constitute some degree of
431 generalization by leveraging the measurements made during the aircraft campaigns. As for the
432 differences in the vertical shapes (i.e., the curvature) of the sensitivity of the retrievals between
433 HCHO and NO₂ channels (i.e., ~340 nm and ~440 nm), under normal atmospheric and viewing
434 geometry conditions, several studies such as Nowlan et al. 2018 and Lorente et al. 2017 showed
435 small differences in the vertical shapes of the scattering weights in the first few kilometers altitude
436 above the surface where the significant fluctuations in FNRs usually take place. Therefore, our
437 analysis does not consider the varying vertical shapes in the scattering weights. However, this
438 assumption might not hold for excessive aerosol loading with variable extinction efficiency
439 between ~340 nm and ~440 nm wavelengths or extreme solar zenith angles.

440 Figure 5 demonstrates the violin plot of the afternoon (> 12:00 LT) vertical distribution of
441 HCHO, NO₂, and FNR observed by NASA's aircraft during the four field campaigns analyzed in
442 this study superimposed by the simulated PO₃ rates. The vertical layers are grouped into sixteen

443 altitudes ranging from 0.25 km to 7.75 km. Each vertical layer incorporates measurements ± 0.25
 444 km of the mid-layer height. The observations do not follow a normal distribution, particularly in
 445 the lower parts of the atmosphere; thus, medians are preferred to represent the central tendency.
 446 While the largest PO_3 rates tend to occur in areas close to the surface (< 2 km agl), a nonnegligible
 447 fraction of the elevated PO_3 rates are also observed in other parts of the atmosphere, such as in the
 448 free troposphere.

449 Several intriguing features are observed in Figure 5: First, up to the 5.75 km range, which
 450 encompasses the PBL area and a large portion of the free troposphere, NO_2 concentrations tend to
 451 decrease quicker than those of HCHO in line with previous studies such as Schroeder et al. (2017),
 452 Jin et al. (2017), Chan et al. (2019), and Ren et al. (2022). Second, above 5.75 km, HCHO levels
 453 off, whereas NO_2 shows an increasing trend. Finally, due to their different vertical shapes, we
 454 observe nonuniformities in the vertical distribution of FNR: they become more NO_x -sensitive with
 455 altitude up to a turning point at 5.75 km and then shift back to the VOC-sensitive direction.

456 It is attractive to model these shapes and apply parameterizations to understand how their
 457 shapes will complicate the use of tropospheric column retrieval from satellites. First order rational
 458 functions are a good candidate to use. Concerning the vertical dependency of HCHO and NO_2 , we
 459 find reasonable fit ($R^2=0.73$) as:

$$HCHO, NO_2 = \frac{a_0 z + a_1}{z + a_2} \quad (7)$$

460 where z is altitude in km. a_i ($i=0,1,2$) are fitting parameters. From this equation it is determined
 461 that FNRs follow a second order rational function:

$$f(z) = \frac{HCHO}{NO_2} = \frac{b_0 z^2 + b_1 z + b_2}{b_3 z^2 + b_4 z + b_5} \quad (8)$$

462 where b_i ($i=0, \dots, 5$) are fitting parameters. One can effortlessly fit this function to different bounds
 463 of the vertical distribution of FNR such as the 25th and 75th percentiles, and subsequently estimate
 464 the first moment of the resultant polygon along z divided by the total area bounded to the polygon
 465 (the centroid, G) via:

$$G(z_1, z_2) = \frac{1}{2A} \int_{z_1}^{z_2} f^2(z)_{75th} - f^2(z)_{25th} dz \quad (9)$$

466 where A is the area of the polygon bounded by the 75th percentiles, $f(z)_{75th}$, and the 25th
 467 percentiles ($f(z)_{25th}$) of FNR (shown in Figure 5 as solid black lines). We define an altitude
 468 adjustment factor (f_{adj}) such that one can translate an observed FNR tropospheric column ratios,
 469 such as those retrieved from satellites, to a defined altitude and below that point (z_t) through:

$$f_{adj} = \frac{G(0, z_t)}{G(0, 8 \text{ km})} \quad (10)$$

470 where z_t can be interchanged to match the PBLH. This definition is more beneficial than using the
 471 entire tropospheric column to the surface conversion (e.g., Jin et al., 2017) because ozone can form
 472 in various vertical layers. Using the observations collected during the campaign, we estimate Eq.
 473 (10) along with $\pm 1\sigma$ boundaries shown in Figure 6. To determine the adjustment factor error, we
 474 reestimate Eq.9 with $\pm 1\sigma$ level in the coefficients obtained from Eq.8. The resultant error is shown
 475 in the dashed red line in Figure 6. This error results from uncertainties associated with assuming
 476 that the second-order rational function can explain the vertical distribution of FNRs. The shape of
 477 the resulting adjustment factor is in line with the vertical distribution of FNR (see Figure 5): the
 478 adjustment factor curve closer to the surface has values smaller than one, increases to values larger
 479 than one in the mid-troposphere, and finally, converges to one near the top of measured
 480 concentrations. If one picks out an altitude pertaining to a PBLH, one can easily apply f_{adj} to the

481 observed FNR columns to estimate the corresponding ratio for that specific PBLH. A more evolved
482 PBLH (i.e., a large z_t) results in stronger vertical mixing, rendering f_{adj} closer to one. The standard
483 error deviation of this conversion is around 19%. The relatively low fluctuations in the adjustment
484 factor around one suggest that under the observed atmospheric conditions (clear-sky afternoon
485 summers), the columnar tropospheric ratios do not poorly represent the chemical conditions in the
486 PBL region.

487 It is beneficial to model this curve to make this data-driven conversion easier for future
488 applications. A second-order polynomial can well describe ($R^2=0.97$) this curve:

$$f_{\text{adj}} = az_t^2 + bz_t + c \quad a = -0.01, b = 0.15, c = 0.78 \quad (11)$$

489 Although Eq. (11) does not include observations above 8 km, the area bounded between $f(z)_{75\text{th}}$
490 and $f(z)_{25\text{th}}$ in higher altitudes is too small to make a noticeable impact on this adjustment factor.

491 One may object that since we estimated the adjustment factor based on two boundaries
492 (25th and 75th percentiles) of the data, we are no longer really dealing with 50% of features
493 observed in the vertical shapes of FNR. This valid critique can be overcome by gradually relaxing
494 the lower and upper limits and examining the resulting change in f_{adj} . When we reduce the lower
495 limit in Eq. (9) from the 25th to 1st percentiles, the optimal curve is similar to the one shown in
496 Figure 6 (Figure S12). However, when we extend the upper limit from the 75th percentile to greater
497 values, we see the fit becoming less robust above the 80th percentile, indicating that the formulation
498 applies to ~80% of the data. The reason behind the poor representation of the adjustment factor
499 for the upper tail of the population is the extremely steep turning point between 5.5 and 6.0 km,
500 necessitating a higher-order rational function to be used for Eq. (7) and Eq. (8). We prefer to limit
501 this analysis to both boundaries and the order defined in Eq. (8) and Eq. (9) because extreme value
502 predictions usually lack robustness.

503 A caveat with these results is that our analysis is limited to afternoon observations because
504 we focus on afternoon low-orbiting sensors such as OMI and TROPOMI. Nonetheless, Schroeder
505 et al. (2017) and Crawford et al. (2021) observed large diurnal variability in these profiles due to
506 diurnal variability in sinks and sources of NO₂ and HCHO and atmospheric dynamics. The diurnal
507 cycle has an important implication for geostationary satellites such as Tropospheric Emissions
508 indeed: Monitoring of Pollution (TEMPO) (Chance et al., 2019). Limiting the observations to
509 morning time results in a smaller adjustment factor for altitudes close to the surface resulting from
510 steeper vertical gradients of HCHO/NO₂ (Figures S13 and S14). This tendency agrees with Jin et
511 al. (2017), who observed a larger deviation from one in an adjustment factor used for the column-
512 surface conversion in winter.

513 Another important caveat with our analysis is that it is based upon four air quality
514 campaigns in warm seasons that avoid times/areas with convective transport; as such, our analysis
515 needs to be made aware of the vertical shapes of FNR during convective activities and cold
516 seasons. However, a few compelling assumptions can minimize these oversights: first, it is very
517 atypical to encounter elevated ozone production rates during cold seasons with few exceptions
518 (Ahmadov et al., 2015; Rappenglück et al., 2014); second, the notion of ozone regimes is only
519 appropriate in photochemically active environments where the ROx-HOx cycle is active; an
520 example of this can be found in Souri et al. (2021) who observed an enhancement of surface ozone
521 in central Europe during a lockdown in April 2020 (up to 5 ppbv) compared to a baseline which
522 was explainable by the reduced O₃ titration through NO in place of the photochemically induced
523 production. An exaggerated extension to this example is the nighttime chemistry where NO-O₃-
524 NO₂ partitioning is the primary driver of negative ozone production rates; at night, the definition
525 of NOx-sensitive or VOC-sensitive is meaningless, so it is in photochemically less active

526 environments; third, it is rarely advisable to use cloudy scenes in satellite UV-Vis gas retrievals
 527 due to the arguable assumption on Lambertian clouds and highly uncertain cloud optical centroid
 528 and albedo; accordingly, atmospheric convection occurring during storms or fires is commonly
 529 masked in satellite-based studies. Therefore, the limitations associated with the adjustment factor
 530 are mild compared to the advantages.

531 **3.6. Spatial Heterogeneity**

532 The spatial representation error resulting from unresolved processes and scales (Janić et
 533 al., 2016; Valin et al., 2011; Souri et al., 2022) refers to the amount of information lost due to
 534 satellite footprint or unresolved inputs used in satellite retrieval algorithms. Unfortunately, this
 535 source of error cannot be determined when we do not know the true state of the spatial variability.
 536 There is, however, a practical way to resolve this by conducting multi-scale intercomparisons of a
 537 coarse spatial resolution output against a finer one. Yet, despite the absence of the truth in this
 538 approach, we tend to find their comparisons useful in giving us an appreciation of the error.

539 We build the reference data on qualified pixels ($qa_value > 0.75$) of offline TROPOMI
 540 tropospheric NO_2 version 2.2.0 (van Geffen et al., 2021; Boersma et al., 2018) and total HCHO
 541 columns version 2.02.01 (De Smedt et al., 2018) oversampled at $3 \times 3 \text{ km}^2$ in summer 2021 over
 542 the US. Figure 7 shows the map of those tropospheric columns as well as FNR. Encouragingly,
 543 the small footprint and relatively low detection limit of TROPOMI compared to its predecessor
 544 satellite sensors (e.g., OMI) enable us to have possibly one of the finest maps of HCHO over the
 545 US to date. Large values of HCHO columns are found in the southeast due to strong isoprene
 546 emissions (e.g., Zhu et al., 2016; Wells et al., 2020). Cities like Houston (Boeke et al., 2011; Zhu
 547 et al., 2014; Pan et al., 2015; Diao et al., 2016), Kansas City, Phoenix (Nunnermacker et al., 2004),
 548 and Los Angeles (de Gouw et al., 2018) also show pronounced enhancements of HCHO possibly
 549 due to anthropogenic sources. Expectedly, large tropospheric NO_2 columns are often confined to
 550 cities and some coal-fired power plants along the Ohio River basin. Concerning FNR, low values
 551 dominate cities, whereas high values are found in remote regions. An immediate tendency
 552 observed from these maps is that the length scale of HCHO columns is longer than that of NO_2 .
 553 This indicates that NO_2 columns are more heterogeneous. Because of this, we observe a large
 554 degree of spatial heterogeneity with respect to FNRs.

555 Here we limit our analysis to Los Angeles due to computational costs imposed by the
 556 subsequent experiment. To quantify the spatial representation errors caused by satellite footprint
 557 size, we upscale the FNRs by convolving the values with four low pass box filters with the size of
 558 13×24 , 36×36 , 108×108 , and $216 \times 216 \text{ km}^2$, shown in the first column of Figure 8. Subsequently,
 559 to extract the spatial variance (information), we follow the definition of the experimental
 560 semivariogram (Matheron, 1963):

$$561 \quad \gamma(\mathbf{h}) = \frac{1}{2N(\mathbf{h})} \sum_{|x_i - x_j| - |\mathbf{h}| \leq \varepsilon} [Z(x_i) - Z(x_j)]^2 \quad (12)$$

562 where $Z(x_i)$ (and $Z(x_j)$) is discrete pixels of FNRs, $N(\mathbf{h})$ is the number of paired pixels separated
 563 by the vector of \mathbf{h} . The $|\cdot|$ operator indicates the length of a vector. The condition of $|x_i - x_j| -$
 564 $|\mathbf{h}| \leq \varepsilon$ is to permit certain tolerance for differences in the length of the vector. Here, we ignore
 565 the directional dependence in $\gamma(\mathbf{h})$ which makes the vector of \mathbf{h} scalar ($h = |\mathbf{h}|$). Moreover, we bin
 566 γ values in 100 evenly-spaced intervals ranging from 0 to 5 degrees. To remove potential outliers
 567 (such as noise), it is wise to model the semivariogram using an empirical regression model. To
 model the semivariogram, we follow the stable Gaussian function used by Souri et al. (2022):

$$\gamma(h) = s(1 - e^{-\frac{h}{r}c_0}); c_0=1.5 \quad (13)$$

568 where r and s are fitting parameters. For the most part, geophysical quantities become spatially
 569 uncorrelated at a certain distance called the range, and the variance associated with that distance
 570 is called the sill. The fitting parameters, r , and s , describe these two quantities as long as the stable
 571 Gaussian function can well fit to the shape of semivariogram. The semivariograms, and the fits,
 572 associated with each map are depicted in the second column of Figure 8.

573 The modeled semivariograms suggest that a coarser field comes with a smaller sill,
 574 implying a loss in the spatial information (variance). The length scale (i.e., the range) only sharply
 575 increases at coarser footprints ($>36 \times 36 \text{ km}^2$). This indicates that several coarse-resolution satellite
 576 sensors, such as OMI ($13 \times 24 \text{ km}^2$), are rather able to determine the length scales of FNR over a
 577 major city such as Los Angeles. By leveraging the modeled semivariograms, we can effortlessly
 578 determine the spatial representation error for specific scale (e.g., $h=10 \text{ km}$) through

$$e^2(h) = 1 - \frac{\gamma(h)}{\gamma_{ref}(h)} \quad (14)$$

579 where $\gamma(h)$ and $\gamma_{ref}(h)$ are the modeled semivariogram of the target and the reference fields (3×3
 580 km^2). This equation articulates the amount of information lost in the target field compared to the
 581 reference. Accordingly, the proposed formulation of the spatial representation error is relative.
 582 Figure 9 depicts the representation errors for various footprints. For the most part, the OMI nadir
 583 pixel ($13 \times 24 \text{ km}^2$) only has a $\sim 12\%$ loss of the spatial variance. On the contrary, a grid box with a
 584 size of $216 \times 216 \text{ km}^2$ fails at capturing $\sim 65\%$ of the spatial information in FNR with a 50 km length
 585 scale comparable to the extent of Los Angeles. The advantage of our method is that we can
 586 mathematically describe the spatial representation error as a function of the length of our target.
 587 The present method can be easily applied to other atmospheric compounds and locations. We have
 588 named this method SpaTial Representation Error EstimaTor (STREET) which is publicly available
 589 as an open-source package (Souri, 2022).

590 An oversight in the above experiment lies in its lack of appreciation of unresolved physical
 591 processes in the satellite measurements: a weak sensitivity of some retrievals to the near-surface
 592 pollution due to the choice of spectral windows used for fitting (Yang et al., 2014), using 1-D air
 593 mass factor calculation instead of 3-D (Schwaerzel et al., 2020), and neglecting aerosol effect on
 594 the light path are just a few examples to point out. To account for the unresolved processes, one
 595 can recalculate Eqs. (12)-(14) using outputs from different retrieval frameworks, which is beyond
 596 the scope of this study.

597 **3.7. Satellite errors**

598 **3.7.1. Concept**

599 Two types of retrieval errors can affect our analysis: systematic errors (bias) and
 600 unsystematic ones (random errors). In theory, it is very compelling to understand their differences.
 601 In reality, the distinction between random and systematic errors is not as clear-cut as it seems. For
 602 example, one may wish to establish the credibility of a satellite retrieval by comparing it to a sky-
 603 radiance measurement over time. Because each measurement is made at a different time, their
 604 comparison is not a repetition of the same experiment; each time, the atmosphere differs in some
 605 aspects, so each comparison is unique. Adding more sky-radiance measurements will add new
 606 experiments. For each paired data point, many unique issues contribute differently to errors; as
 607 such, our problem is grossly under-determined (i.e., more unknowns for a given observation).

608 Here, we do not attempt to separate random from systematic errors in the subsequent analysis,
609 thereby limiting this study to the total uncertainty.

610 We focus on analyzing the statistical errors drawn from the differences between the
611 benchmark and the retrievals on daily basis. Two sensors are used for this analysis: TROPOMI
612 and OMI. To propagate individual uncertainties in HCHO and NO₂ to FNRs, we follow an
613 analytical approach involving Jacobians of the ratio to HCHO and NO₂. Assuming that errors in
614 HCHO and NO₂ are uncorrelated, the relative error of the ratio can be estimated by:

$$\frac{\sigma}{ratio} = \sqrt{\left(\frac{\sigma_{HCHO}}{HCHO}\right)^2 + \left(\frac{\sigma_{NO_2}}{NO_2}\right)^2} \quad (15)$$

615 where σ_{HCHO} and σ_{NO_2} are total uncertainties of HCHO and NO₂ observations. It is important to
616 recognize that the errors in HCHO and NO₂ are not strictly uncorrelated due to assumptions made
617 in their air mass factor calculations.

618 3.7.2. Error Distributions in TROPOMI and OMI

619 We begin our analysis with the error distribution of daily TROPOMI tropospheric NO₂
620 columns (v1.02.02) against 22 MAX-DOAS instruments from May to September in 2018-2021.
621 The data are paired based on the criteria defined in Verhoelst et al. (2021). The spatial locations
622 of the stations are mapped in Figure S15. Figure 10a shows the histogram of the TROPOMI minus
623 the MAX-DOAS instruments. The first observation from this distribution is that it is skewed
624 towards lower differences, evident in the skewness parameter around -4.6. As a result of the
625 skewness, the median should better represent the central tendency which is around -1×10^{15}
626 molec./cm². In general, TROPOMI tropospheric NO₂ columns show a low bias. We fit a normal
627 distribution to the data using the non-linear Levenberg-Marquardt method. This fitted normal
628 distribution ($R^2=0.94$) is used to approximate σ_{NO_2} for different confidence intervals, and to
629 minimize blunders. To understand how much of these disagreements are caused by systematic
630 errors as opposed to random errors, we redo the histogram using monthly-based observations
631 (Figure S16). A slight change in the dispersions between the daily and the monthly-basis analysis
632 indicates the significance of unresolved systematic (or relative) biases. This tendency suggests that
633 when conducting the analysis on a monthly basis, the relative bias cannot be mitigated by
634 averaging. Verhoelst et al. (2021) rigorously studied the potential root cause of some discrepancies
635 between MAX-DOAS and TROPOMI. An important source of error stems from the fundamental
636 differences in the vertical sensitivities of MAX-DOAS (more sensitive to the lower tropospheric
637 region) and TROPOMI (more sensitive to the upper tropospheric area). This systematic error can
638 only be mitigated using reliably high-resolution vertical shape factors instead of spatiotemporal
639 averaging of the satellite data.

640 The error analysis for OMI follows the same methods applied for TROPOMI; however,
641 with different benchmarks. We follow the comparisons made between the operational product
642 version 3.1 and measured columns derived from NCAR's NO₂ measurements integrated along
643 aircraft spirals during four NASA's air quality campaigns. More information regarding this data
644 comparison can be found in Choi et al. (2020). Figure 10b shows the histogram of OMI minus the
645 integrated spirals. Compared to TROPOMI, the OMI bias is worse by a factor of two. The standard
646 deviation calculated from a Gaussian fit (2.31×10^{15} molec./cm²) is not substantially different from
647 that of TROPOMI (2.11×10^{15} molec./cm²).

648 As for the error distribution of TROPOMI HCHO columns (version 1.1.(5-7)), we use 24
649 FTIR measurements during the same time period based on the criteria specified in Vigouroux et

650 al. (2020). The stations are mapped in Figure S15. The frequency of the paired data is daily. Figure
651 11a depicts the error distribution. The distribution is slightly broader compared to that of NO₂,
652 manifested in a larger standard deviation 4.32×10^{15} molec./cm². This is primarily due to two facts:
653 i) HCHO optical depths generally peak in the UV range (<380 nm), where the large optical depths
654 of ozone and Rayleigh scattering result in weaker and noisier signals (Gonzalez Abad et al., 2019),
655 and ii) the broader and stronger NO₂ optical depths in the ViS range (400-500 nm), where the
656 signal-to-noise ratio is typically more outstanding, permit better quality retrievals. Similar to the
657 NO₂, we fit a normal distribution ($R^2=0.90$) to specify σ_{HCHO} for different confidence intervals.

658 Concerning OMI HCHO columns from SAO version 3 (Gonzalez Abad et al., 2015), we
659 follow the intercomparison approach proposed in Zhu et al. (2020). Based on this approach, the
660 benchmarks come from GEOS-Chem simulated HCHO columns corrected by in-situ aircraft
661 measurements. The measurements were made during ozone seasons from KORUS-AQ,
662 DISCOVERs, FRAPPE, NOMADSS, and SENEX campaigns (see Table 1 in Zhu et al. 2020).
663 OMI values ranging from -0.5×10^{15} molec./cm² and 1.0×10^{17} molec./cm² with effective cloud
664 fraction between 0.0 and 0.3, and SZA between 0 and 60 degrees are only considered in the
665 comparison. Any pixels from OMI and grid boxes from the corrected GEOS-Chem simulation that
666 fall into a polygon enclosing the campaign domain are used to create the error distribution shown
667 in Figure 11b. The distribution has much denser data because the model output covers a large
668 portion of the satellite swath. The error distribution suggests that OMI HCHO is inferior to
669 TROPOMI evident in larger bias and standard deviation. The OMI bias is twice as large as that of
670 TROPOMI. De Smedt et al. (2021) observed the same level of bias from their comparisons of
671 OMI/TROPOMI with MAX-DOAS instruments (see Table 3 in their paper). Moreover, their OMI
672 vs MAX-DOAS comparisons were severely scattered. Likewise, we observe the standard deviation
673 of OMI from the fitted Gaussian function to be roughly five times as large of that TROPOMI. This
674 can be primarily due to a weaker signal-to-noise (and sensor degradation) in OMI. It is because of
675 this reason that OMI HCHO should be averaged over several months. Another possible reason for
676 the large standard deviation is the fact that the benchmark arises from a modeling experiment
677 whose ability at resolving spatiotemporal variations in HCHO may be uncertain. This partly leads
678 to the performance of OMI to look poor.

679 3.7.3. *The impact of retrieval error on the ratio*

680 Following Eq. (15), we calculate the standard error for a wide range of NO₂ and HCHO
681 columns at a 68% confidence interval (1 sigma) for both TROPOMI and OMI derived from the
682 fitted Gaussian function to the histograms; the standard errors are shown in Figure 12. We observe
683 smaller errors to be associated with larger tropospheric column concentrations. As for TROPOMI,
684 either daily HCHO or tropospheric NO₂ columns should be above $1.2-1.5 \times 10^{16}$ molec./cm² to
685 achieve 20-30% standard error. The TROPOMI errors start diminishing the application of FNR
686 when both measurements are below this threshold. Regarding OMI, it is nearly impossible to get
687 the standard error below of 20-30% given its problematically large HCHO standard deviation. For
688 50% error, the daily HCHO columns should be above 3.2×10^{16} molec./cm². This range of error
689 can also be achieved if OMI tropospheric NO₂ columns are above 8×10^{15} molec./cm².

690 3.8. *The fractional errors to the combined error*

691 The ultimate task is to compile the aforementioned errors to gauge how each individual
692 source of error contributes to the overall error. Although each error is different in nature, combined
693 they explain the uncertainties of one quantity (FNR) and can be roughly considered independent;
694 therefore, the combined error is given by:

$$\sigma_{total} = \sqrt{\sigma_{Col2PBL}^2 + \sigma_{SpatialRep}^2 + \sigma_{Retrieval}^2} \quad (16)$$

695 $\sigma_{Col2PBL}$ is the error in the adjustment-factor defined in this study. We calculated a 26% standard
 696 error for a wide range of PBLHs. Therefore, $\sigma_{Col2PBL}$ equals to 19% of the observed ratio (i.e.,
 697 magnitude dependent). $\sigma_{SpatialRep}$ is more complex. It is a function of the footprint of the satellite
 698 (or a model), the spatial variability of the reference field, which varies from environment to
 699 environment, and the length scale of our target (e.g., a district, a city, or a state). Eq. (14) explicitly
 700 quantifies this error. The product of the square root of that value and the observed ratio defines
 701 $\sigma_{SpatialRep}$. The last error depends on the magnitude of HCHO and NO₂ tropospheric columns. It
 702 can be estimated from Eq. (15) times the observed ratio. We did not include the chemistry error in
 703 Eq. (16) because it was suited only for segregating the chemical conditions; it does not describe
 704 the level of uncertainties that comes with the observed columnar ratio. Figure 13 shows the total
 705 relative error given the observed TROPOMI ratio seen in Figure 7. We consider the OMI spatial
 706 representation error (13% variance loss) for this case that was computed in a city environment.
 707 The retrieval errors are based on TROPOMI sigma values. Areas associated with relatively small
 708 errors (<50%) are mostly seen in cities due to a stronger signal (smaller $\sigma_{Retrieval}$). Places with
 709 low vegetation and anthropogenic sources (i.e., Rocky Mountains) possess the largest errors
 710 (>100%).

711 To produce some examples of the fractional errors to the combined error, we focus on two
 712 different environments with two different sets of HCHO and NO₂ columns. One represents a
 713 heavily polluted area, and the other one is a moderately polluted region. We also include two
 714 footprints: OMI (13×24 km²) and a 108×108 km² pixel. Finally, we calculate the percentage of
 715 each error component for both OMI and TROPOMI sensors. Figure 14 shows the pie charts
 716 describing the percentage of each individual error to the total error for TROPOMI. Unless the
 717 footprint of the sensor is coarse enough (e.g., 108 km²) to give rise to the spatial representation
 718 error dominance, the retrieval error stands out. New satellites are not expected to have very large
 719 footprints; as such, retrieval errors appear to be the major obstacle to using FNR in a robust
 720 manner. Figure 15 shows the same calculation but using OMI errors; the retrieval errors massively
 721 surpass other errors. This motivates us to do one more experiment; we recalculate the HCHO error
 722 distribution in OMI using monthly-averaged data instead of daily (Figure S17). This experiment
 723 suggests a standard deviation of 9.4×10^{15} molec./cm², with which we again observe the retrieval
 724 error to be the largest contributor (>80%) of the combined error (Figure S18). A recent study
 725 (Johnson et al., 2022) also suggests that retrieval errors can result in considerable disagreement
 726 between FNRs from various sensors and retrieval frameworks.

727 4. Summary

728 The main goal of this study was to characterize the errors associated with the ratio of
 729 satellite-based HCHO to NO₂ columns, which has been widely used for ozone sensitivity studies.
 730 From the realization of the complexity of the problem, we now know that four major errors should
 731 be carefully quantified so that we can reliably represent the underlying ozone regimes. The errors
 732 are broken down into i) the chemistry error, ii) the column to the PBL translation, iii) the spatial
 733 representation error, and iv) the retrieval error. Each error has its own dynamics and has been
 734 tackled differently by leveraging a broad spectrum of tools and data.

735 The chemistry error refers to the predictive power of the HCHO/NO₂ ratio (hereafter FNR)
 736 in describing the HO_x-RO_x cycle, which can be well explained by the ratio of the chemical loss

737 of HO₂+RO₂ (LRO_x) to the chemical loss of NO_x (LNO_x). Because those chemical reactions are
738 not directly observable, we set up a chemical box model constrained with a large suite of in-situ
739 aircraft measurements collected during DISCOVER-AQs and KORUS-AQ campaigns (~ 500 hr
740 of flight). Our box model showed a reasonable performance at recreating some unconstrained key
741 compounds such as OH (R²=0.64, bias=17%), HO₂ (R²=0.66, bias<1%), and HCHO (R²=0.73).
742 Subsequently, we compared the simulated FNRs to LRO_x/LNO_x. They showed a high degree of
743 correspondence (R²=0.93) but only in the logarithmic scale; this indicated that FNRs do not fully
744 describe the HO_x-RO_x cycle (i.e., the sensitivity of ozone production rates to NO_x and VOC) for
745 heavily polluted environments and pristine ones. Following a robust baseline indicator
746 ($\ln(\text{LRO}_x/\text{LNO}_x) = -1.0 \pm 0.2$) segregating NO_x-sensitive from VOC-sensitive regimes, we
747 observed a diverse range of FNR ranging from 1 to 4. These transitioning ratios had a Gaussian
748 distribution with a mean of 1.8 and a standard deviation of 0.4. This implied that the relative
749 standard error associated with the ratio from the chemistry perspective at a 68% confidence interval
750 was 20%. Although this threshold with its error was based on a single model realization and can
751 be different for a different chemical mechanism, it provided a useful universal baseline derived
752 from various chemical and meteorological conditions. At a 68% confidence level, any uncertainty
753 beyond 20% in the ozone regime identification from FNRs likely originates from other sources of
754 error, such as the retrieval error.

755 Results from the box model showed that ozone production rates in extremely polluted
756 regions (VOC-sensitive) were not significantly different from those in pristine ones (NO_x-
757 sensitive) due to non-linear chemical feedback mostly imposed by NO₂+OH. Indeed, the largest
758 PO₃ rates (median = 4.6 ppbv/hr) were predominantly seen in VOC-sensitive regimes tending
759 towards the transitional regime. This was primarily caused by the abundance of ozone precursors
760 (i.e., HCHO×NO₂) and the diminished negative chemical feedback. We also revealed that
761 HCHO×NO₂ could be used as a sensible proxy for the ozone precursors' abundance. In theory,
762 this metric, in conjunction with the ratio, provided reasonable estimates of PO₃ rates (RMSE =
763 0.60 ppbv/hr).

764 We then analyzed the afternoon vertical distribution of HCHO, NO₂, and their ratio
765 observed from aircraft during the air quality campaigns binned to the near-surface to 8 km. For
766 altitudes below 5.75 km, HCHO concentration steadily decreased with altitude but at a lower rate
767 than NO₂. Above that altitude, NO₂ concentrations stabilized and slightly increased due to
768 lightning and stratospheric sources. The dissimilarity between the vertical shape of NO₂ versus
769 HCHO resulted in a rather non-linear shape of FNR. This non-linear shape necessitated a
770 mathematical formulation to transform an observed columnar ratio to a ratio at a desired vertical
771 height expanding from the surface. We fit a second-order rational function to the profile and
772 formulated the altitude adjustment factor, which followed a second-order polynomial function
773 starting from values below 1 for lower altitudes, following values above 1 for some high altitudes,
774 and finally converging to 1 at 8 km. This behavior means that the ozone regime tends to get pushed
775 slightly towards the VOC-sensitive regime near the surface for a given tropospheric columnar
776 ratio. This tendency was more pronounced in morning times when the non-linear shape of FNRs
777 was stronger. This data-driven adjustment factor exclusively derived from afternoon aircraft
778 profiles during warm seasons in non-convective conditions had a standard error of 19%.

779 An important error in the satellite-based observations stemmed from unresolved spatial
780 variability in trace gas concentrations within a satellite pixel (Souri et al., 2022; Tang et al., 2021).
781 The amount of unresolved spatial variability (the spatial representation error) can in principle be
782 modeled if we base our reference on a distribution map made from a high spatial resolution dataset.

783 We modeled semivariograms (or spatial auto-correlation) computed for a reference map of FNR
784 observed by TROPOMI at $3\times 3\text{ km}^2$ over Los Angeles. Subsequently, we coarsened the map to
785 13×24 , 36×36 , 108×108 , and $216\times 216\text{ km}^2$ and modeled their semivariograms. As for $13\times 24\text{ km}^2$,
786 which is equivalent to the OMI nadir spatial resolution, around 12% of spatial information
787 (variance) was lost due to its footprint. The larger the footprint, the bigger the spatial representation
788 error. For instance, a grid box with a size of $216\times 216\text{ km}^2$ lost 65% of the spatial information in
789 the ratio at a 50 km length scale. Our method is compelling to understand and easy to apply for
790 other products and different atmospheric environments. Based on this approach, we developed an
791 open-source package called SpaTial Representation Error EstimaTor (STREET) (Souri, 2022).

792 We presented estimates of retrieval errors associated with daily TROPOMI and OMI
793 tropospheric NO_2 columns by comparing them against a large suite of MAX-DOAS (Verhoelst et
794 al. 2021) and vertically-integrated measurements from aircraft spirals (Choi et al., 2020). Both
795 products were smaller than the benchmark. Furthermore, they show a relatively consistent
796 dispersion at a 68% confidence level ($\sim 2\times 10^{15}\text{ molec./cm}^2$) suggested by fitting a normal function
797 ($R^2>0.9$) to their error distributions. As for daily TROPOMI and OMI HCHO products, we used
798 global FTIR observations (Vigouroux et al., 2020) and data-constrained GEOS-Chem outputs from
799 multiple campaigns (Zhu et al., 2020), respectively. TROPOMI HCHO indeed outperforms OMI
800 HCHO with respect to bias and dispersion on a daily basis. The standard deviation of OMI HCHO
801 was found to be roughly five times as large compared to TROPOMI. While this error can be partly
802 reduced by oversampling over a span of a month or a season, it is critical to recognize that ozone
803 events are episodic; thus, daily observations should be the standard mean for understanding the
804 chemical pathways for the formation of tropospheric ozone. After combining the daily biases from
805 both HCHO and NO_2 TROPOMI comparisons, we concluded that either daily HCHO or
806 tropospheric NO_2 columns should be above $1.2\text{-}1.5\times 10^{16}\text{ molec./cm}^2$ to achieve 20-30% standard
807 error in the ratio. Due to the large error in daily OMI HCHO, it was nearly impossible to achieve
808 20-30% standard error given the observable range of HCHO and NO_2 columns over our planet. To
809 reach 50% error using daily OMI data, HCHO columns should be above $3.2\times 10^{16}\text{ molec./cm}^2$ or
810 tropospheric NO_2 columns should be above $8\times 10^{15}\text{ molec./cm}^2$.

811 To build intuition in the significance of the errors above, we finally calculated the
812 combined error in the ratio by linearly combining the root sum of the squares of the TROPOMI
813 retrieval errors, the spatial representation error pertaining to OMI nadir footprint over a city-like
814 environment, and the altitude adjustment error for a wide range of observed HCHO and NO_2
815 columns over the US. These observations were based on the TROPOMI in the summertime of
816 2021. The total errors were relatively mild ($<50\%$) in cities due to a stronger signal, whereas they
817 easily exceeded 100% in regions with low vegetation and anthropogenic sources (i.e., Rocky
818 Mountains). The retrieval error was the dominant source of the combined error (40-90%).

819 All of these aspects highlight the necessity of improving the trace gas satellite retrieval
820 algorithms in conjunction with sensor calibration, although with the realization that a better
821 retrieval is somewhat limited by the advancements made in other disciplines, such as atmospheric
822 modeling and molecular spectroscopy.

823 **Acknowledgment**

824 This study was funded by NASA's Aura Science Team (grant number: 80NSSC21K1333). PTR-
825 MS measurements were supported by the Austrian Federal Ministry for Transport, Innovation and
826 Technology (bmvit, FFG-ALR-ASAP). The PTR-MS instrument team (P. Eichler, L. Kaser, T.
827 Mikoviny, M. Müller) is acknowledged for their support with field work and data processing. We
828 acknowledge FTIR HCHO measurements team including T. Blumenstock, M. De Mazière, M.

829 Grutter, J. W. Hannigan, N. Jones, R. Kivi, E. Lutsch, E. Mahieu, M. Makarova, I. Morino, I.
830 Murata, T. Nagahama, J. Notholt, I. Ortega, M. Palm, A. Röhling, M. Schneider, D. Smale, W.
831 Stremme, K. Strong, Y. Sun, R. Sussmann, Y. Té, and P. Wang. The measurements at Paramaribo
832 have been supported by the BMBF (German Ministry of Education and Research) in the project
833 ROMIC-II subproject TroStra (01LG1904A). The NDACC FTIR stations Bremen, Garmisch,
834 Izaña, Ny-Ålesund, Paramaribo and Karlsruhe have been supported by the German
835 Bundesministerium für Wirtschaft und Energie (BMWi) via DLR under grants 50EE1711A, B and
836 D. We thank the Meteorological Service Suriname and Cornelis Becker for support. The
837 measurements and data analysis at Bremen are supported by the Senate of Bremen. The NCAR
838 FTS observation programs at Thule, GR, Boulder, CO and Mauna Loa, HI are supported under
839 contract by the National Aeronautics and Space Administration (NASA). The National Center for
840 Atmospheric Research is sponsored by the National Science Foundation. The Thule effort is also
841 supported by the NSF Office of Polar Programs (OPP). Operations at the Rikubetsu and Tsukuba
842 FTIR sites are supported in part by the GOSAT series project. The Paris TCCON site has received
843 funding from Sorbonne Université, the French research center CNRS and the French space agency
844 CNES. The Jungfraujoch FTIR data are primarily available thanks to the support provided by the
845 F.R.S. - FNRS (Brussels), the GAW-CH program of MeteoSwiss (Zürich) and the HFSJG.ch
846 Foundation (Bern). The MAX-DOAS data used in this publication were obtained from A. Bais, J.
847 Burrows, K. Chan, M. Grutter, C. Liu, H. Irie, V. Kumar, Y. Kanaya, A. Piters, C. Rivera-
848 Cárdenas, M. Van Roozendaal, R. Ryan, V. Sinha, and T. Wagner. Fast delivery of MAX-DOAS
849 data tailored to the S5P validation was organized through the S5PVT AO project NIDFORVAL.
850 IUP-Bremen ground-based measurements are funded by DLR-Bonn received through project
851 50EE1709A. We thank the IISER Mohali atmospheric chemistry facility for supporting the MAX-
852 DOAS measurements at Mohali, India. KNMI ground-based measurements in De Bilt and Cabauw
853 are partly supported by the Ruisdael Observatory project, Dutch Research Council (NWO) contract
854 184.034.015, by the Netherlands Space Office (NSO) for Sentinel-5p/TROPOMI validation, and
855 by ESA via the EU CAMS-27 project. LZ and SS acknowledge grants from Guangdong Basic and
856 Applied Basic Research Foundation (2021A1515110713) and Shenzhen Science and Technology
857 Program (JCYJ20210324104604012). The TROPOMI validation work was supported by
858 BELSPO/ESA through the ProDEx project TROVA-E2 (grant no. PEA 4000116692). TV
859 acknowledges support from BELSPO through BRAIN-BE 2.0 project LEGO-BEL-AQ (contract
860 B2/191/P1/LEGO-BEL-AQ). We thank Glenn Diskin for providing CO, CO₂, and CH₄
861 measurements. We thank Paul Wennberg for H₂O₂ and HNO₃ measurements.

862

863 **Data Access**

864 The FTIR and MAXDOAS data used in this publication were partly obtained from the Network
865 for the Detection of Atmospheric Composition Change (NDACC) and are available through the
866 NDACC website www.ndacc.org. The spatial representation error is estimated based on publicly
867 available package, SpaTial Representation Error EstimaTor (STREET)
868 (<https://github.com/ahsouri/STREET>). DISCOVER-AQ and KORUS-AQ aircraft data can be
869 downloaded from <https://www-air.larc.nasa.gov/missions/discover-aq/discover-aq.html> and
870 <https://www-air.larc.nasa.gov/missions/korus-aq/>. TROPOMI NO₂ and HCHO data can be
871 downloaded from https://disc.gsfc.nasa.gov/datasets/S5P_L2_NO2_1/summary and
872 https://disc.gsfc.nasa.gov/datasets/S5P_L2_HCHO_1/summary. The box model results can be
873 obtained by contacting the corresponding author through ahsouri@cfa.harvard.edu.

874

875 **Author contributions**

876 AHS designed the research, analyzed the data, conducted the simulations, made all figures, and
877 wrote the paper. MSJ, SP, XL, and KC helped with conceptualization, fundraising, and analysis.
878 GMW helped with configuring the box model. AF, AW, WB, DRB, AJW, RCC, KM, and CC
879 measured various compounds during the air quality campaigns. JHC orchestrated all these
880 campaigns and contributed to the model interpretation. TV, SC, and GP provided paired MAX-
881 DOAS and TROPOMI tropospheric NO₂ observations. CV and BL provided paired FTIR and
882 TROPOMI HCHO observations. SC and LL provided paired integrated aircraft spirals and OMI
883 tropospheric NO₂ observations. LZ and SS provided the paired observations between the corrected
884 GEOS-Chem HCHO and OMI HCHO columns. All authors contributed to the discussion and
885 edited the paper.

886

887

888

889

890

891

892 **References**

- 893 Ahmadov, R., McKeen, S., Trainer, M., Banta, R., Brewer, A., Brown, S., Edwards, P.M., de
894 Gouw, J.A., Frost, G.J., Gilman, J., Helmig, D., Johnson, B., Karion, A., Koss, A.,
895 Langford, A., Lerner, B., Olson, J., Oltmans, S., Peischl, J., Pétron, G., Pichugina, Y.,
896 Roberts, J.M., Ryerson, T., Schnell, R., Senff, C., Sweeney, C., Thompson, C., Veres, P.R.,
897 Warneke, C., Wild, R., Williams, E.J., Yuan, B., Zamora, R., 2015. Understanding high
898 wintertime ozone pollution events in an oil- and natural gas-producing region of the western
899 US. *Atmospheric Chemistry and Physics* 15, 411–429. [https://doi.org/10.5194/acp-15-411-](https://doi.org/10.5194/acp-15-411-2015)
900 [2015](https://doi.org/10.5194/acp-15-411-2015)
- 901 Bela, M.M., Barth, M.C., Toon, O.B., Fried, A., Ziegler, C., Cummings, K.A., Li, Y., Pickering,
902 K.E., Homeyer, C.R., Morrison, H., Yang, Q., Mecikalski, R.M., Carey, L., Biggerstaff,
903 M.I., Betten, D.P., Alford, A.A., 2018. Effects of Scavenging, Entrainment, and Aqueous
904 Chemistry on Peroxides and Formaldehyde in Deep Convective Outflow Over the Central
905 and Southeast United States. *Journal of Geophysical Research: Atmospheres* 123, 7594–
906 7614. <https://doi.org/10.1029/2018JD028271>
- 907 Boeke, N.L., Marshall, J.D., Alvarez, S., Chance, K.V., Fried, A., Kurosu, T.P., Rappenglück, B.,
908 Richter, D., Walega, J., Weibring, P., Millet, D.B., 2011. Formaldehyde columns from the
909 Ozone Monitoring Instrument: Urban versus background levels and evaluation using aircraft
910 data and a global model. *Journal of Geophysical Research: Atmospheres* 116.
911 <https://doi.org/10.1029/2010JD014870>
- 912 Boersma, K.F., Eskes, H.J., Brinksma, E.J., 2004. Error analysis for tropospheric NO₂ retrieval
913 from space. *Journal of Geophysical Research: Atmospheres* 109.
914 <https://doi.org/10.1029/2003JD003962>
- 915 Boersma, K.F., Eskes, H.J., Richter, A., De Smedt, I., Lorente, A., Beirle, S., van Geffen,
916 J.H.G.M., Zara, M., Peters, E., Van Roozendaal, M., Wagner, T., Maasackers, J.D., van der
917 A, R.J., Nightingale, J., De Rudder, A., Irie, H., Pinardi, G., Lambert, J.-C., Compernelle,
918 S.C., 2018. Improving algorithms and uncertainty estimates for satellite NO₂ retrievals:
919 results from the quality assurance for the essential climate variables (QA4ECV) project.
920 *Atmospheric Measurement Techniques* 11, 6651–6678. [https://doi.org/10.5194/amt-11-](https://doi.org/10.5194/amt-11-6651-2018)
921 [6651-2018](https://doi.org/10.5194/amt-11-6651-2018)
- 922 Boersma, K.F., Eskes, H.J., Veefkind, J.P., Brinksma, E.J., van der A, R.J., Sneep, M., van den
923 Oord, G.H.J., Levelt, P.F., Stammes, P., Gleason, J.F., Bucsela, E.J., 2007. Near-real time
924 retrieval of tropospheric NO₂ from OMI. *Atmospheric Chemistry and Physics* 7, 2103–
925 2118. <https://doi.org/10.5194/acp-7-2103-2007>
- 926 Box, G.E.P., 1976. Science and Statistics. *Journal of the American Statistical Association* 71,
927 791–799. <https://doi.org/10.1080/01621459.1976.10480949>
- 928 Brune, W.H., Miller, D.O., Thames, A.B., Brosius, A.L., Barletta, B., Blake, D.R., Blake, N.J.,
929 Chen, G., Choi, Y., Crawford, J.H., Digangi, J.P., Diskin, G., Fried, A., Hall, S.R., Hanisco,
930 T.F., Huey, G.L., Hughes, S.C., Kim, M., Meinardi, S., Montzka, D.D., Pusede, S.E.,
931 Schroeder, J.R., Teng, A., Tanner, D.J., Ullmann, K., Walega, J., Weinheimer, A.,
932 Wisthaler, A., Wennberg, P.O., 2022. Observations of atmospheric oxidation and ozone
933 production in South Korea. *Atmospheric Environment* 269, 118854.
934 <https://doi.org/10.1016/j.atmosenv.2021.118854>
- 935 Chan, K.L., Wang, Z., Ding, A., Heue, K.-P., Shen, Y., Wang, J., Zhang, F., Shi, Y., Hao, N.,
936 Wenig, M., 2019. MAX-DOAS measurements of tropospheric NO₂ and HCHO in Nanjing

937 and a comparison to ozone monitoring instrument observations. *Atmospheric Chemistry and*
938 *Physics* 19, 10051–10071. <https://doi.org/10.5194/acp-19-10051-2019>

939 Chance, K., Palmer, P.I., Spurr, R.J.D., Martin, R.V., Kurosu, T.P., Jacob, D.J., 2000. Satellite
940 observations of formaldehyde over North America from GOME. *Geophysical Research*
941 *Letters* 27, 3461–3464. <https://doi.org/10.1029/2000GL011857>

942 Chance, K., Liu, X., Miller, C.C., Abad, G.G., Huang, G., Nowlan, C., Souri, A., Suleiman, R.,
943 Sun, K., Wang, H., Zhu, L., Zoogman, P., Al-Saadi, J., Antuña-Marrero, J.-C., Carr, J.,
944 Chatfield, R., Chin, M., Cohen, R., Edwards, D., Fishman, J., Flittner, D., Geddes, J.,
945 Grutter, M., Herman, J.R., Jacob, D.J., Janz, S., Joiner, J., Kim, J., Krotkov, N.A., Lefer, B.,
946 Martin, R.V., Mayol-Bracero, O.L., Naeger, A., Newchurch, M., Pfister, G.G., Pickering,
947 K., Pierce, R.B., Cárdenas, C.R., Saiz-Lopez, A., Simpson, W., Spinei, E., Spurr, R.J.D.,
948 Szykman, J.J., Torres, O., Wang, J., 2019. TEMPO Green Paper: Chemistry, physics, and
949 meteorology experiments with the Tropospheric Emissions: monitoring of pollution
950 instrument, in: *Sensors, Systems, and Next-Generation Satellites XXIII*. Presented at the
951 *Sensors, Systems, and Next-Generation Satellites XXIII*, SPIE, pp. 56–67.
952 <https://doi.org/10.1117/12.2534883>

953 Chance, K.V., Burrows, J.P., Perner, D., Schneider, W., 1997. Satellite measurements of
954 atmospheric ozone profiles, including tropospheric ozone, from ultraviolet/visible
955 measurements in the nadir geometry: a potential method to retrieve tropospheric ozone.
956 *Journal of Quantitative Spectroscopy and Radiative Transfer* 57, 467–476.
957 [https://doi.org/10.1016/S0022-4073\(96\)00157-4](https://doi.org/10.1016/S0022-4073(96)00157-4)

958 Chance, K.V., Burrows, J.P., Schneider, W., 1991. Retrieval and molecule sensitivity studies for
959 the global ozone monitoring experiment and the scanning imaging absorption spectrometer
960 for atmospheric cartography, in: *Remote Sensing of Atmospheric Chemistry*. Presented at
961 the *Remote Sensing of Atmospheric Chemistry*, SPIE, pp. 151–165.
962 <https://doi.org/10.1117/12.46657>

963 Choi, S., Lamsal, L.N., Follette-Cook, M., Joiner, J., Krotkov, N.A., Swartz, W.H., Pickering,
964 K.E., Loughner, C.P., Appel, W., Pfister, G., Saide, P.E., Cohen, R.C., Weinheimer, A.J.,
965 Herman, J.R., 2020. Assessment of NO₂ observations during DISCOVER-AQ and KORUS-
966 AQ field campaigns. *Atmospheric Measurement Techniques* 13, 2523–2546.
967 <https://doi.org/10.5194/amt-13-2523-2020>

968 Choi, Y., Kim, H., Tong, D., Lee, P., 2012b. Summertime weekly cycles of observed and
969 modeled NO_x and O₃ concentrations as a function of satellite-derived ozone production
970 sensitivity and land use types over the Continental United States. *Atmospheric Chemistry*
971 *and Physics* 12, 6291–6307. <https://doi.org/10.5194/acp-12-6291-2012>

972 Choi, Y., Souri, A.H., 2015a. Seasonal behavior and long-term trends of tropospheric ozone, its
973 precursors and chemical conditions over Iran: A view from space. *Atmospheric*
974 *Environment* 106, 232–240. <https://doi.org/10.1016/j.atmosenv.2015.02.012>

975 Choi, Y., Souri, A.H., 2015b. Chemical condition and surface ozone in large cities of Texas
976 during the last decade: Observational evidence from OMI, CAMS, and model analysis.
977 *Remote Sensing of Environment* 168, 90–101. <https://doi.org/10.1016/j.rse.2015.06.026>

978 Crawford, J.H., Ahn, J.-Y., Al-Saadi, J., Chang, L., Emmons, L.K., Kim, J., Lee, G., Park, J.-H.,
979 Park, R.J., Woo, J.H., Song, C.-K., Hong, J.-H., Hong, Y.-D., Lefer, B.L., Lee, M., Lee, T.,
980 Kim, S., Min, K.-E., Yum, S.S., Shin, H.J., Kim, Y.-W., Choi, J.-S., Park, J.-S., Szykman,
981 J.J., Long, R.W., Jordan, C.E., Simpson, I.J., Fried, A., Dibb, J.E., Cho, S., Kim, Y.P., 2021.

982 The Korea–United States Air Quality (KORUS-AQ) field study. *Elementa: Science of the*
983 *Anthropocene* 9, 00163. <https://doi.org/10.1525/elementa.2020.00163>

984 de Gouw, J.A., Gilman, J.B., Kim, S.-W., Alvarez, S.L., Dusanter, S., Graus, M., Griffith, S.M.,
985 Isaacman-VanWertz, G., Kuster, W.C., Lefer, B.L., Lerner, B.M., McDonald, B.C.,
986 Rappenglück, B., Roberts, J.M., Stevens, P.S., Stutz, J., Thalman, R., Veres, P.R.,
987 Volkamer, R., Warneke, C., Washenfelder, R.A., Young, C.J., 2018. Chemistry of Volatile
988 Organic Compounds in the Los Angeles Basin: Formation of Oxygenated Compounds and
989 Determination of Emission Ratios. *Journal of Geophysical Research: Atmospheres* 123,
990 2298–2319. <https://doi.org/10.1002/2017JD027976>

991 De Smedt, I., Müller, J.-F., Stavrou, T., van der A, R., Eskes, H., Van Roozendaal, M., 2008.
992 Twelve years of global observations of formaldehyde in the troposphere using GOME and
993 SCIAMACHY sensors. *Atmospheric Chemistry and Physics* 8, 4947–4963.
994 <https://doi.org/10.5194/acp-8-4947-2008>

995 De Smedt, I., Pinardi, G., Vigouroux, C., Compernelle, S., Bais, A., Benavent, N., Boersma, F.,
996 Chan, K.-L., Donner, S., Eichmann, K.-U., Hedelt, P., Hendrick, F., Irie, H., Kumar, V.,
997 Lambert, J.-C., Langerock, B., Lerot, C., Liu, C., Loyola, D., PETERS, A., Richter, A., Rivera
998 Cárdenas, C., Romahn, F., Ryan, R.G., Sinha, V., Theys, N., Vlietinck, J., Wagner, T.,
999 Wang, T., Yu, H., Van Roozendaal, M., 2021. Comparative assessment of TROPOMI and
1000 OMI formaldehyde observations and validation against MAX-DOAS network column
1001 measurements. *Atmospheric Chemistry and Physics* 21, 12561–12593.
1002 <https://doi.org/10.5194/acp-21-12561-2021>

1003 De Smedt, I., Stavrou, T., Hendrick, F., Danckaert, T., Vlemmix, T., Pinardi, G., Theys, N.,
1004 Lerot, C., Gielen, C., Vigouroux, C., Hermans, C., Fayt, C., Veeffkind, P., Müller, J.-F., Van
1005 Roozendaal, M., 2015. Diurnal, seasonal and long-term variations of global formaldehyde
1006 columns inferred from combined OMI and GOME-2 observations. *Atmospheric Chemistry*
1007 *and Physics* 15, 12519–12545. <https://doi.org/10.5194/acp-15-12519-2015>

1008 De Smedt, I., Stavrou, T., Müller, J.-F., van der A, R.J., Van Roozendaal, M., 2010. Trend
1009 detection in satellite observations of formaldehyde tropospheric columns. *Geophysical*
1010 *Research Letters* 37. <https://doi.org/10.1029/2010GL044245>

1011 De Smedt, I., Theys, N., Yu, H., Danckaert, T., Lerot, C., Compernelle, S., Van Roozendaal, M.,
1012 Richter, A., Hilboll, A., Peters, E., Pedernana, M., Loyola, D., Beirle, S., Wagner, T.,
1013 Eskes, H., van Geffen, J., Boersma, K.F., Veeffkind, P., 2018. Algorithm theoretical baseline
1014 for formaldehyde retrievals from S5P TROPOMI and from the QA4ECV project.
1015 *Atmospheric Measurement Techniques* 11, 2395–2426. [https://doi.org/10.5194/amt-11-](https://doi.org/10.5194/amt-11-2395-2018)
1016 [2395-2018](https://doi.org/10.5194/amt-11-2395-2018)

1017 Diao, L., Choi, Y., Czader, B., Li, X., Pan, S., Roy, A., Souri, A.H., Estes, M., Jeon, W., 2016.
1018 Discrepancies between modeled and observed nocturnal isoprene in an urban environment
1019 and the possible causes: A case study in Houston. *Atmospheric Research* 181, 257–264.
1020 <https://doi.org/10.1016/j.atmosres.2016.07.009>

1021 Duncan, B.N., Yoshida, Y., Olson, J.R., Sillman, S., Martin, R.V., Lamsal, L., Hu, Y., Pickering,
1022 K.E., Retscher, C., Allen, D.J., Crawford, J.H., 2010. Application of OMI observations to a
1023 space-based indicator of NO_x and VOC controls on surface ozone formation. *Atmospheric*
1024 *Environment* 44, 2213–2223. <https://doi.org/10.1016/j.atmosenv.2010.03.010>

1025 Fried, A., Walega, J., Weibring, P., Richter, D., Simpson, I.J., Blake, D.R., Blake, N.J., Meinardi,
1026 S., Barletta, B., Hughes, S.C., Crawford, J.H., Diskin, G., Barrick, J., Hair, J., Fenn, M.,
1027 Wisthaler, A., Mikoviny, T., Woo, J.-H., Park, M., Kim, Jinseok, Min, K.-E., Jeong, S.,

1028 Wennberg, P.O., Kim, M.J., Crouse, J.D., Teng, A.P., Bennett, R., Yang-Martin, M.,
1029 Shook, M.A., Huey, G., Tanner, D., Knote, C., Kim, JongHo, Park, R., Brune, W., 2020.
1030 Airborne formaldehyde and volatile organic compound measurements over the Daesan
1031 petrochemical complex on Korea's northwest coast during the Korea-United States Air
1032 Quality study: Estimation of emission fluxes and effects on air quality. *Elementa: Science of*
1033 *the Anthropocene* 8, 121. <https://doi.org/10.1525/elementa.2020.121>

1034 González Abad, G., Liu, X., Chance, K., Wang, H., Kurosu, T.P., Suleiman, R., 2015. Updated
1035 Smithsonian Astrophysical Observatory Ozone Monitoring Instrument (SAO OMI)
1036 formaldehyde retrieval. *Atmospheric Measurement Techniques* 8, 19–32.
1037 <https://doi.org/10.5194/amt-8-19-2015>

1038 Gonzalez Abad, G., Souri, A.H., Bak, J., Chance, K., Flynn, L.E., Krotkov, N.A., Lamsal, L., Li,
1039 C., Liu, X., Miller, C.C., Nowlan, C.R., Suleiman, R., Wang, H., 2019. Five decades
1040 observing Earth's atmospheric trace gases using ultraviolet and visible backscatter solar
1041 radiation from space. *Journal of Quantitative Spectroscopy and Radiative Transfer* 238,
1042 106478. <https://doi.org/10.1016/j.jqsrt.2019.04.030>

1043 Janjić, T., Bormann, N., Bocquet, M., Carton, J.A., Cohn, S.E., Dance, S.L., Losa, S.N., Nichols,
1044 N.K., Potthast, R., Waller, J.A., Weston, P., 2018. On the representation error in data
1045 assimilation. *Quarterly Journal of the Royal Meteorological Society* 144, 1257–1278.
1046 <https://doi.org/10.1002/qj.3130>

1047 Jeon, W., Choi, Y., Souri, A.H., Roy, A., Diao, L., Pan, S., Lee, H.W., Lee, S.-H., 2018.
1048 Identification of chemical fingerprints in long-range transport of burning induced upper
1049 tropospheric ozone from Colorado to the North Atlantic Ocean. *Science of The Total*
1050 *Environment* 613–614, 820–828. <https://doi.org/10.1016/j.scitotenv.2017.09.177>

1051 Jin, X., Fiore, A.M., Murray, L.T., Valin, L.C., Lamsal, L.N., Duncan, B., Folkert Boersma, K.,
1052 De Smedt, I., Abad, G.G., Chance, K., Tonnesen, G.S., 2017. Evaluating a Space-Based
1053 Indicator of Surface Ozone-NO_x-VOC Sensitivity Over Midlatitude Source Regions and
1054 Application to Decadal Trends. *Journal of Geophysical Research: Atmospheres* 122,
1055 10,439-10,461. <https://doi.org/10.1002/2017JD026720>

1056 Jin, X., Holloway, T., 2015. Spatial and temporal variability of ozone sensitivity over China
1057 observed from the Ozone Monitoring Instrument. *Journal of Geophysical Research:*
1058 *Atmospheres* 120, 7229–7246. <https://doi.org/10.1002/2015JD023250>

1059 Kleinman, L.I., Daum, P.H., Lee, Y.-N., Nunnermacker, L.J., Springston, S.R., Weinstein-Lloyd,
1060 J., Rudolph, J., 2001. Sensitivity of ozone production rate to ozone precursors. *Geophysical*
1061 *Research Letters* 28, 2903–2906. <https://doi.org/10.1029/2000GL012597>

1062 Laughner, J.L., Zhu, Q., Cohen, R.C., 2019. Evaluation of version 3.0B of the BEHR OMI NO₂
1063 product. *Atmospheric Measurement Techniques* 12, 129–146. [https://doi.org/10.5194/amt-](https://doi.org/10.5194/amt-12-129-2019)
1064 [12-129-2019](https://doi.org/10.5194/amt-12-129-2019)

1065 Lee, H.-J., Chang, L.-S., Jaffe, D.A., Bak, J., Liu, X., Abad, G.G., Jo, H.-Y., Jo, Y.-J., Lee, J.-B.,
1066 Yang, G.-H., Kim, J.-M., Kim, C.-H., 2022. Satellite-Based Diagnosis and Numerical
1067 Verification of Ozone Formation Regimes over Nine Megacities in East Asia. *Remote*
1068 *Sensing* 14, 1285. <https://doi.org/10.3390/rs14051285>

1069 Lee, Y., Huey, L.G., Wang, Y., Qu, H., Zhang, R., Ji, Y., Tanner, D.J., Wang, X., Tang, J., Song,
1070 W., Hu, W., Zhang, Y., 2021. Photochemistry of Volatile Organic Compounds in the
1071 Yellow River Delta, China: Formation of O₃ and Peroxyacyl Nitrates. *Journal of*
1072 *Geophysical Research: Atmospheres* 126, e2021JD035296.
1073 <https://doi.org/10.1029/2021JD035296>

1074 Lorente, A., Folkert Boersma, K., Yu, H., Dörner, S., Hilboll, A., Richter, A., Liu, M., Lamsal,
1075 L.N., Barkley, M., De Smedt, I., Van Roozendael, M., Wang, Y., Wagner, T., Beirle, S.,
1076 Lin, J.-T., Krotkov, N., Stammes, P., Wang, P., Eskes, H.J., Krol, M., 2017. Structural
1077 uncertainty in air mass factor calculation for NO₂ and HCHO satellite retrievals.
1078 Atmospheric Measurement Techniques 10, 759–782. [https://doi.org/10.5194/amt-10-759-](https://doi.org/10.5194/amt-10-759-2017)
1079 [2017](https://doi.org/10.5194/amt-10-759-2017)

1080 Martin, R.V., Chance, K., Jacob, D.J., Kurosu, T.P., Spurr, R.J.D., Bucsela, E., Gleason, J.F.,
1081 Palmer, P.I., Bey, I., Fiore, A.M., Li, Q., Yantosca, R.M., Koelemeijer, R.B.A., 2002. An
1082 improved retrieval of tropospheric nitrogen dioxide from GOME. Journal of Geophysical
1083 Research: Atmospheres 107, ACH 9-1-ACH 9-21. <https://doi.org/10.1029/2001JD001027>

1084 Martin, R.V., Fiore, A.M., Van Donkelaar, A., 2004. Space-based diagnosis of surface ozone
1085 sensitivity to anthropogenic emissions. Geophysical Research Letters 31.
1086 <https://doi.org/10.1029/2004GL019416>

1087 Matheron, G., 1963. Principles of geostatistics. Economic Geology 58, 1246–1266.
1088 <https://doi.org/10.2113/gsecongeo.58.8.1246>

1089 Miller, D.O., Brune, W.H., 2022. Investigating the Understanding of Oxidation Chemistry Using
1090 20 Years of Airborne OH and HO₂ Observations. Journal of Geophysical Research:
1091 Atmospheres 127, e2021JD035368. <https://doi.org/10.1029/2021JD035368>

1092 Newland, M.J., Bryant, D.J., Dunmore, R.E., Bannan, T.J., Acton, W.J.F., Langford, B.,
1093 Hopkins, J.R., Squires, F.A., Dixon, W., Drysdale, W.S., Ivatt, P.D., Evans, M.J., Edwards,
1094 P.M., Whalley, L.K., Heard, D.E., Slater, E.J., Woodward-Massey, R., Ye, C., Mehra, A.,
1095 Worrall, S.D., Bacak, A., Coe, H., Percival, C.J., Hewitt, C.N., Lee, J.D., Cui, T., Surratt,
1096 J.D., Wang, X., Lewis, A.C., Rickard, A.R., Hamilton, J.F., 2021. Low-NO atmospheric
1097 oxidation pathways in a polluted megacity. Atmospheric Chemistry and Physics 21, 1613–
1098 1625. <https://doi.org/10.5194/acp-21-1613-2021>

1099 Nowlan, C.R., Liu, X., Janz, S.J., Kowalewski, M.G., Chance, K., Follette-Cook, M.B., Fried, A.,
1100 González Abad, G., Herman, J.R., Judd, L.M., Kwon, H.-A., Loughner, C.P., Pickering,
1101 K.E., Richter, D., Spinei, E., Walega, J., Weibring, P., Weinheimer, A.J., 2018. Nitrogen
1102 dioxide and formaldehyde measurements from the GEOstationary Coastal and Air Pollution
1103 Events (GEO-CAPE) Airborne Simulator over Houston, Texas. Atmospheric Measurement
1104 Techniques 11, 5941–5964. <https://doi.org/10.5194/amt-11-5941-2018>

1105 Nunnermacker, L.J., Weinstein-Lloyd, J., Kleinman, L., Daum, P.H., Lee, Y.N., Springston,
1106 S.R., Klotz, P., Newman, L., Neuroth, G., Hyde, P., 2004. Ground-based and aircraft
1107 measurements of trace gases in Phoenix, Arizona (1998). Atmospheric Environment 38,
1108 4941–4956. <https://doi.org/10.1016/j.atmosenv.2004.04.033>

1109 Pan, S., Choi, Y., Roy, A., Li, X., Jeon, W., Souri, A.H., 2015. Modeling the uncertainty of
1110 several VOC and its impact on simulated VOC and ozone in Houston, Texas. Atmospheric
1111 Environment 120, 404–416. <https://doi.org/10.1016/j.atmosenv.2015.09.029>

1112 Rappenglück, B., Ackermann, L., Alvarez, S., Golovko, J., Buhr, M., Field, R.A., Soltis, J.,
1113 Montague, D.C., Hauze, B., Adamson, S., Risch, D., Wilkerson, G., Bush, D., Stoeckenius,
1114 T., Keslar, C., 2014. Strong wintertime ozone events in the Upper Green River basin,
1115 Wyoming. Atmospheric Chemistry and Physics 14, 4909–4934. [https://doi.org/10.5194/acp-](https://doi.org/10.5194/acp-14-4909-2014)
1116 [14-4909-2014](https://doi.org/10.5194/acp-14-4909-2014)

1117 Ren, B., Xie, P., Xu, J., Li, A., Qin, M., Hu, R., Zhang, T., Fan, G., Tian, X., Zhu, W., Hu, Z.,
1118 Huang, Y., Li, X., Meng, F., Zhang, G., Tong, J., Ren, H., Zheng, J., Zhang, Z., Lv, Y.,
1119 2022. Vertical characteristics of NO₂ and HCHO, and the ozone formation regimes in

1120 Hefei, China. *Science of The Total Environment* 823, 153425.
1121 <https://doi.org/10.1016/j.scitotenv.2022.153425>

1122 Schroeder, J.R., Crawford, J.H., Fried, A., Walega, J., Weinheimer, A., Wisthaler, A., Müller,
1123 M., Mikoviny, T., Chen, G., Shook, M., Blake, D.R., Tonnesen, G.S., 2017. New insights
1124 into the column CH₂O/NO₂ ratio as an indicator of near-surface ozone sensitivity. *Journal*
1125 *of Geophysical Research: Atmospheres* 122, 8885–8907.
1126 <https://doi.org/10.1002/2017JD026781>

1127 Schroeder, J.R., Crawford, J.H., Ahn, J.-Y., Chang, L., Fried, A., Walega, J., Weinheimer, A.,
1128 Montzka, D.D., Hall, S.R., Ullmann, K., Wisthaler, A., Mikoviny, T., Chen, G., Blake,
1129 D.R., Blake, N.J., Hughes, S.C., Meinardi, S., Diskin, G., Digangi, J.P., Choi, Y., Pusede,
1130 S.E., Huey, G.L., Tanner, D.J., Kim, M., Wennberg, P., 2020. Observation-based modeling
1131 of ozone chemistry in the Seoul metropolitan area during the Korea-United States Air
1132 Quality Study (KORUS-AQ). *Elementa: Science of the Anthropocene* 8, 3.
1133 <https://doi.org/10.1525/elementa.400>

1134

1135 Schwaerzel, M., Emde, C., Brunner, D., Morales, R., Wagner, T., Berne, A., Buchmann, B.,
1136 Kuhlmann, G., 2020. Three-dimensional radiative transfer effects on airborne and ground-
1137 based trace gas remote sensing. *Atmospheric Measurement Techniques* 13, 4277–4293.
1138 <https://doi.org/10.5194/amt-13-4277-2020>

1139 Seinfeld, J. H. and Pandis, S. N., 2006: *Atmospheric Chemistry and Physics: From Air Pollution*
1140 *to Climate Change*, 2nd Edn., Wiley-Interscience, Hoboken, N.J., ISBN: 978-1-118-94740-
1141 1.

1142 Sillman, S., He, D., 2002. Some theoretical results concerning O₃-NO_x-VOC chemistry and
1143 NO_x-VOC indicators. *Journal of Geophysical Research: Atmospheres* 107, ACH 26-1-ACH
1144 26-15. <https://doi.org/10.1029/2001JD001123>

1145 Sillman, S., Logan, J.A., Wofsy, S.C., 1990. The sensitivity of ozone to nitrogen oxides and
1146 hydrocarbons in regional ozone episodes. *Journal of Geophysical Research: Atmospheres*
1147 95, 1837–1851. <https://doi.org/10.1029/JD095iD02p01837>

1148 Souri, A.H., Chance, K., Bak, J., Nowlan, C.R., González Abad, G., Jung, Y., Wong, D.C., Mao,
1149 J., Liu, X., 2021. Unraveling pathways of elevated ozone induced by the 2020 lockdown in
1150 Europe by an observationally constrained regional model using TROPOMI. *Atmospheric*
1151 *Chemistry and Physics* 21, 18227–18245. <https://doi.org/10.5194/acp-21-18227-2021>

1152 Souri, A.H., Chance, K., Sun, K., Liu, X., Johnson, M.S., 2022. Dealing with spatial
1153 heterogeneity in pointwise-to-gridded- data comparisons. *Atmospheric Measurement*
1154 *Techniques* 15, 41–59. <https://doi.org/10.5194/amt-15-41-2022>

1155 Souri, A.H., Nowlan, C.R., Wolfe, G.M., Lamsal, L.N., Chan Miller, C.E., Abad, G.G., Janz,
1156 S.J., Fried, A., Blake, D.R., Weinheimer, A.J., Diskin, G.S., Liu, X., Chance, K., 2020.
1157 Revisiting the effectiveness of HCHO/NO₂ ratios for inferring ozone sensitivity to its
1158 precursors using high resolution airborne remote sensing observations in a high ozone
1159 episode during the KORUS-AQ campaign. *Atmospheric Environment* 224, 117341.
1160 <https://doi.org/10.1016/j.atmosenv.2020.117341>

1161 Souri. (2022). ahsouri/STREET: STREET 0.0.2 (0.0.2). Zenodo.
1162 <https://doi.org/10.5281/zenodo.6993116>

1163 Tang, W., Edwards, D.P., Emmons, L.K., Worden, H.M., Judd, L.M., Lamsal, L.N., Al-Saadi,
1164 J.A., Janz, S.J., Crawford, J.H., Deeter, M.N., Pfister, G., Buchholz, R.R., Gaubert, B.,
1165 Nowlan, C.R., 2021. Assessing sub-grid variability within satellite pixels over urban regions

1166 using airborne mapping spectrometer measurements. *Atmospheric Measurement Techniques*
1167 14, 4639–4655. <https://doi.org/10.5194/amt-14-4639-2021>

1168 Thornton, J.A., Wooldridge, P.J., Cohen, R.C., Martinez, M., Harder, H., Brune, W.H., Williams,
1169 E.J., Roberts, J.M., Fehsenfeld, F.C., Hall, S.R., Shetter, R.E., Wert, B.P., Fried, A., 2002.
1170 Ozone production rates as a function of NO_x abundances and HO_x production rates in the
1171 Nashville urban plume. *Journal of Geophysical Research: Atmospheres* 107, ACH 7-1-ACH
1172 7-17. <https://doi.org/10.1029/2001JD000932>

1173 Tonnesen, G.S., Dennis, R.L., 2000a. Analysis of radical propagation efficiency to assess ozone
1174 sensitivity to hydrocarbons and NO_x : 1. Local indicators of instantaneous odd oxygen
1175 production sensitivity. *Journal of Geophysical Research: Atmospheres* 105, 9213–9225.
1176 <https://doi.org/10.1029/1999JD900371>

1177 Tonnesen, G.S., Dennis, R.L., 2000b. Analysis of radical propagation efficiency to assess ozone
1178 sensitivity to hydrocarbons and NO_x : 2. Long-lived species as indicators of ozone
1179 concentration sensitivity. *Journal of Geophysical Research: Atmospheres* 105, 9227–9241.
1180 <https://doi.org/10.1029/1999JD900372>

1181 Valin, L.C., Russell, A.R., Hudman, R.C., Cohen, R.C., 2011. Effects of model resolution on the
1182 interpretation of satellite NO₂ observations. *Atmospheric Chemistry and Physics* 11,
1183 11647–11655. <https://doi.org/10.5194/acp-11-11647-2011>

1184 van Geffen, J., Eskes, H., Compornolle, S., Pinardi, G., Verhoelst, T., Lambert, J.-C., Sneep, M.,
1185 ter Linden, M., Ludewig, A., Boersma, K.F., Veefkind, J.P., 2022. Sentinel-5P TROPOMI
1186 NO₂ retrieval: impact of version v2.2 improvements and comparisons with OMI and
1187 ground-based data. *Atmospheric Measurement Techniques* 15, 2037–2060.
1188 <https://doi.org/10.5194/amt-15-2037-2022>

1189 Verhoelst, T., Compornolle, S., Pinardi, G., Lambert, J.-C., Eskes, H.J., Eichmann, K.-U.,
1190 Fjæraa, A.M., Granville, J., Niemeijer, S., Cede, A., Tiefengraber, M., Hendrick, F.,
1191 Pazmiño, A., Bais, A., Bazureau, A., Boersma, K.F., Bogner, K., Dehn, A., Donner, S.,
1192 Elokhov, A., Gebetsberger, M., Goutail, F., Grutter de la Mora, M., Gruzdev, A., Gratsea,
1193 M., Hansen, G.H., Irie, H., Jepsen, N., Kanaya, Y., Karagkiozidis, D., Kivi, R., Kreher, K.,
1194 Levelt, P.F., Liu, C., Müller, M., Navarro Comas, M., Piders, A.J.M., Pommereau, J.-P.,
1195 Portafaix, T., Prados-Roman, C., Puentedura, O., Querel, R., Remmers, J., Richter, A.,
1196 Rimmer, J., Rivera Cárdenas, C., Saavedra de Miguel, L., Sinyakov, V.P., Stremme, W.,
1197 Strong, K., Van Roozendaal, M., Veefkind, J.P., Wagner, T., Wittrock, F., Yela González,
1198 M., Zehner, C., 2021. Ground-based validation of the Copernicus Sentinel-5P TROPOMI
1199 NO₂ measurements with the NDACC ZSL-DOAS, MAX-DOAS and Pandonia global
1200 networks. *Atmospheric Measurement Techniques* 14, 481–510. [https://doi.org/10.5194/amt-](https://doi.org/10.5194/amt-14-481-2021)
1201 [14-481-2021](https://doi.org/10.5194/amt-14-481-2021)

1202 Vigouroux, C., Langerock, B., Bauer Aquino, C. A., Blumenstock, T., Cheng, Z., De Mazière,
1203 M., De Smedt, I., Grutter, M., Hannigan, J. W., Jones, N., Kivi, R., Loyola, D., Lutsch, E.,
1204 Mahieu, E., Makarova, M., Metzger, J.-M., Morino, I., Murata, I., Nagahama, T., Notholt,
1205 J., Ortega, I., Palm, M., Pinardi, G., Röhling, A., Smale, D., Stremme, W., Strong, K.,
1206 Sussmann, R., Té, Y., van Roozendaal, M., Wang, P., and Winkler, H.: TROPOMI–
1207 Sentinel-5 Precursor formaldehyde validation using an extensive network of ground-based
1208 Fourier-transform infrared stations, *Atmos. Meas. Tech.*, 13, 3751–3767,
1209 <https://doi.org/10.5194/amt-13-3751-2020>, 2020.

1210 Wells, K.C., Millet, D.B., Payne, V.H., Deventer, M.J., Bates, K.H., de Gouw, J.A., Graus, M.,
1211 Warneke, C., Wisthaler, A., Fuentes, J.D., 2020. Satellite isoprene retrievals constrain

1212 emissions and atmospheric oxidation. *Nature* 585, 225–233. <https://doi.org/10.1038/s41586->
1213 [020-2664-3](https://doi.org/10.1038/s41586-020-2664-3)

1214 Wolfe, G. M., Kaiser, J., Hanisco, T.F., Keutsch, F.N., de Gouw, J.A., Gilman, J.B., Graus, M.,
1215 Hatch, C.D., Holloway, J., Horowitz, L.W., Lee, B.H., Lerner, B.M., Lopez-Hilfiker, F.,
1216 Mao, J., Marvin, M.R., Peischl, J., Pollack, I.B., Roberts, J.M., Ryerson, T.B., Thornton,
1217 J.A., Veres, P.R., Warneke, C., 2016. Formaldehyde production from isoprene oxidation
1218 across NO_x regimes. *Atmospheric Chemistry and Physics* 16, 2597–2610.
1219 <https://doi.org/10.5194/acp-16-2597-2016>

1220 Wolfe, Glenn M., Marvin, M.R., Roberts, S.J., Travis, K.R., Liao, J., 2016. The Framework for
1221 0-D Atmospheric Modeling (F0AM) v3.1. *Geoscientific Model Development* 9, 3309–3319.
1222 <https://doi.org/10.5194/gmd-9-3309-2016>

1223 Xu, W., Zhang, G., Wang, Y., Tong, S., Zhang, W., Ma, Z., Lin, W., Kuang, Y., Yin, L., Xu, X.,
1224 2021. Aerosol Promotes Peroxyacetyl Nitrate Formation During Winter in the North China
1225 Plain. *Environ. Sci. Technol.* 55, 3568–3581. <https://doi.org/10.1021/acs.est.0c08157>

1226 Yang, K., Carn, S.A., Ge, C., Wang, J., Dickerson, R.R., 2014. Advancing measurements of
1227 tropospheric NO₂ from space: New algorithm and first global results from OMPS.
1228 *Geophysical Research Letters* 41, 4777–4786. <https://doi.org/10.1002/2014GL060136>

1229 Zhang, K., Duan, Y., Huo, J., Huang, L., Wang, Yangjun, Fu, Q., Wang, Yuhang, Li, L., 2021.
1230 Formation mechanism of HCHO pollution in the suburban Yangtze River Delta region,
1231 China: A box model study and policy implementations. *Atmospheric Environment* 267,
1232 118755. <https://doi.org/10.1016/j.atmosenv.2021.118755>

1233 Zhu, L., González Abad, G., Nowlan, C.R., Chan Miller, C., Chance, K., Apel, E.C., DiGangi,
1234 J.P., Fried, A., Hanisco, T.F., Hornbrook, R.S., Hu, L., Kaiser, J., Keutsch, F.N., Permar,
1235 W., St. Clair, J.M., Wolfe, G.M., 2020. Validation of satellite formaldehyde (HCHO)
1236 retrievals using observations from 12 aircraft campaigns. *Atmospheric Chemistry and*
1237 *Physics* 20, 12329–12345. <https://doi.org/10.5194/acp-20-12329-2020>

1238 Zhu, L., Jacob, D.J., Kim, P.S., Fisher, J.A., Yu, K., Travis, K.R., Mickley, L.J., Yantosca, R.M.,
1239 Sulprizio, M.P., De Smedt, I., González Abad, G., Chance, K., Li, C., Ferrare, R., Fried, A.,
1240 Hair, J.W., Hanisco, T.F., Richter, D., Jo Scarino, A., Walega, J., Weibring, P., Wolfe,
1241 G.M., 2016. Observing atmospheric formaldehyde (HCHO) from space: validation and
1242 intercomparison of six retrievals from four satellites (OMI, GOME2A, GOME2B, OMPS)
1243 with SEAC⁴RS aircraft observations over the southeast US. *Atmospheric Chemistry and*
1244 *Physics* 16, 13477–13490. <https://doi.org/10.5194/acp-16-13477-2016>

1245 Zhu, L., Jacob, D.J., Mickley, L.J., Marais, E.A., Cohan, D.S., Yoshida, Y., Duncan, B.N., Abad,
1246 G.G., Chance, K.V., 2014. Anthropogenic emissions of highly reactive volatile organic
1247 compounds in eastern Texas inferred from oversampling of satellite (OMI) measurements of
1248 HCHO columns. *Environ. Res. Lett.* 9, 114004. <https://doi.org/10.1088/1748->
1249 [9326/9/11/114004](https://doi.org/10.1088/1748-9326/9/11/114004)

1250

1251
1252
1253

Table1. The box model configurations and inputs.

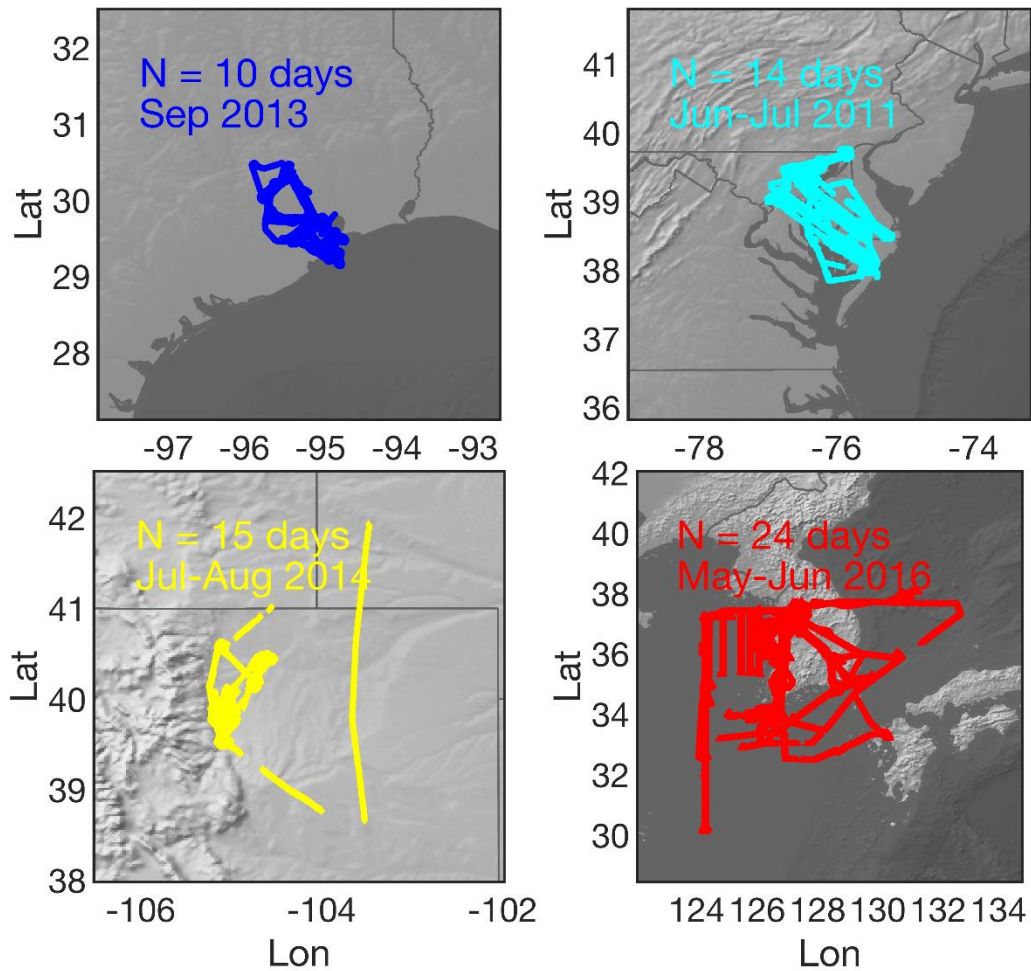
| | |
|--|---|
| Temporal resolution of samples | 10-15 sec |
| Time steps | 1 hour |
| Number of solar cycles | 5 |
| Dilution constant | 1/86400 -1/43200 (s ⁻¹) |
| Meteorological Inputs | Pressure, Temperature, and Relative Humidity |
| Photolysis frequencies estimates | LUT based on the NCAR TUV model calculations |
| Photolysis frequencies constraints (campaign#‡) | Measured jNO ₂ (1-4) and jO ¹ D (4) |
| Compounds (Instrument#†, campaign#‡) used for constraining the box model | H ₂ (1, 4)§, CO (4, 1-4), NO _x (2, 1-4), O ₃ (2, 1-4), SO ₂ (6, 4) , CH ₄ (4, 1-4), HNO ₃ (10, 1-4), Isoprene (9, 1-4), Monoterpenes (9, 1-4), Acetone (9, 1-4), Ethylene (1, 4), Ethane (1, 4), Methanol (9, 1-4), Propane (1, 4), Benzene (1 or 9, 2-4), Xylene (1 or 9, 1 and 4), Toluene (1 or 9, 1-4), Glyoxal (8, 4), Acetaldehyde (9, 1-4), Methyl vinyl ketone (9, 1-4), Methyl Ethyl Ketone (9, 2-4), Propene (1 or 9, 2 and 4), Acetic acid (9, 2-4), Glycolaldehyde (5, 4), H ₂ O ₂ (5, 4) |
| Unconstrained compounds (Instrument#†, campaign#‡) used for validation | HO ₂ (3, 4), OH (3, 4), NO (2, 1-4), NO ₂ (2, 1-4), PAN (10, 1-4), HCHO (7, 1-4) |
| Chemical Mechanism | CB06 |

1254
1255
1256
1257
1258
1259
1260
1261
1262
1263
1264
1265
1266
1267

† (1) UC Irvine's Whole Air Sampler (WAS), (2) NCAR 4-Channel Chemiluminescence, (3) Penn State's Airborne Tropospheric Hydrogen Oxides Sensor (ATHOS), (4) NASA Langley's DACOM tunable diode laser spectrometer, (5) Caltech's single mass analyzer, (6) Georgia Tech's ionization mass spectrometer, (7) The University of Colorado at Boulder's the Compact Atmospheric Multi-species Spectrometer (CAMS), (8) Korean Airborne Cavity Enhances Spectrometer, (9) University of Innsbruck's PTR-TOF-MS instrument, and (10) University of California, Berkeley's TD-LIF.

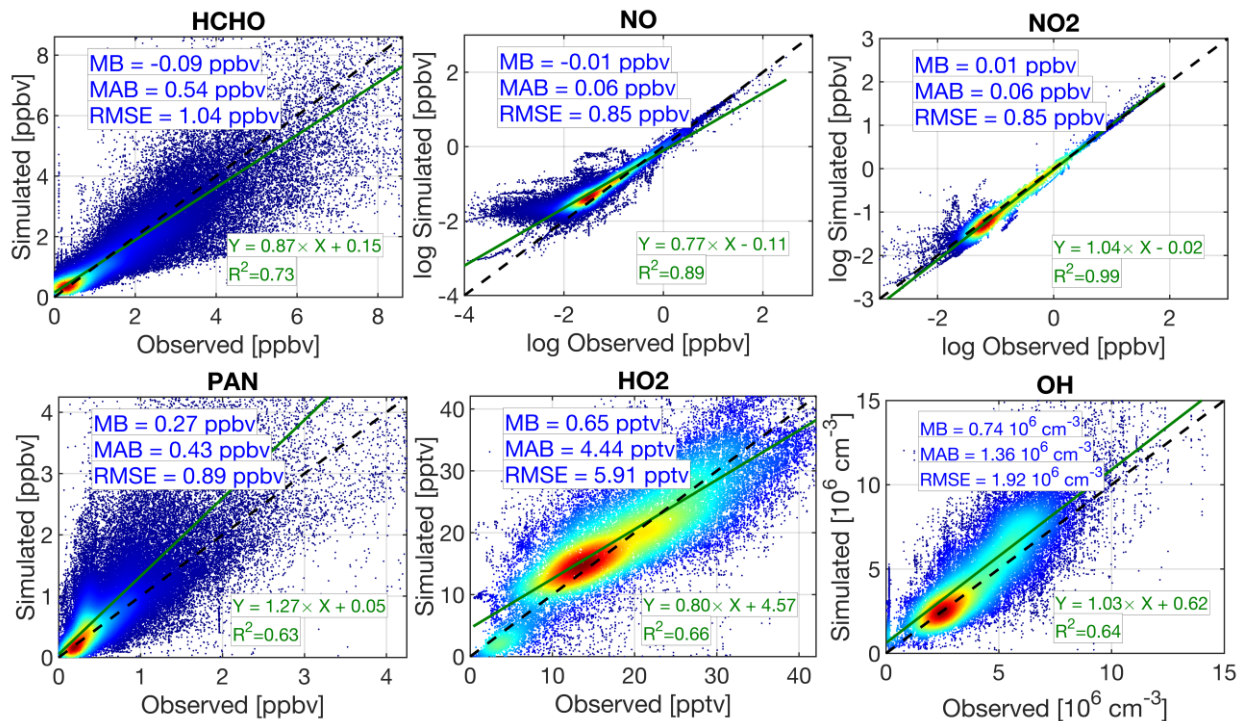
‡ (1) DISCOVER-Baltimore-Washington, (2) DISCOVER-Texas-Houston, (3) DISCOVER-Colorado, and (4) KORUS-AQ

§ In the absence of measurements, a default value of 550 ppbv is specified.



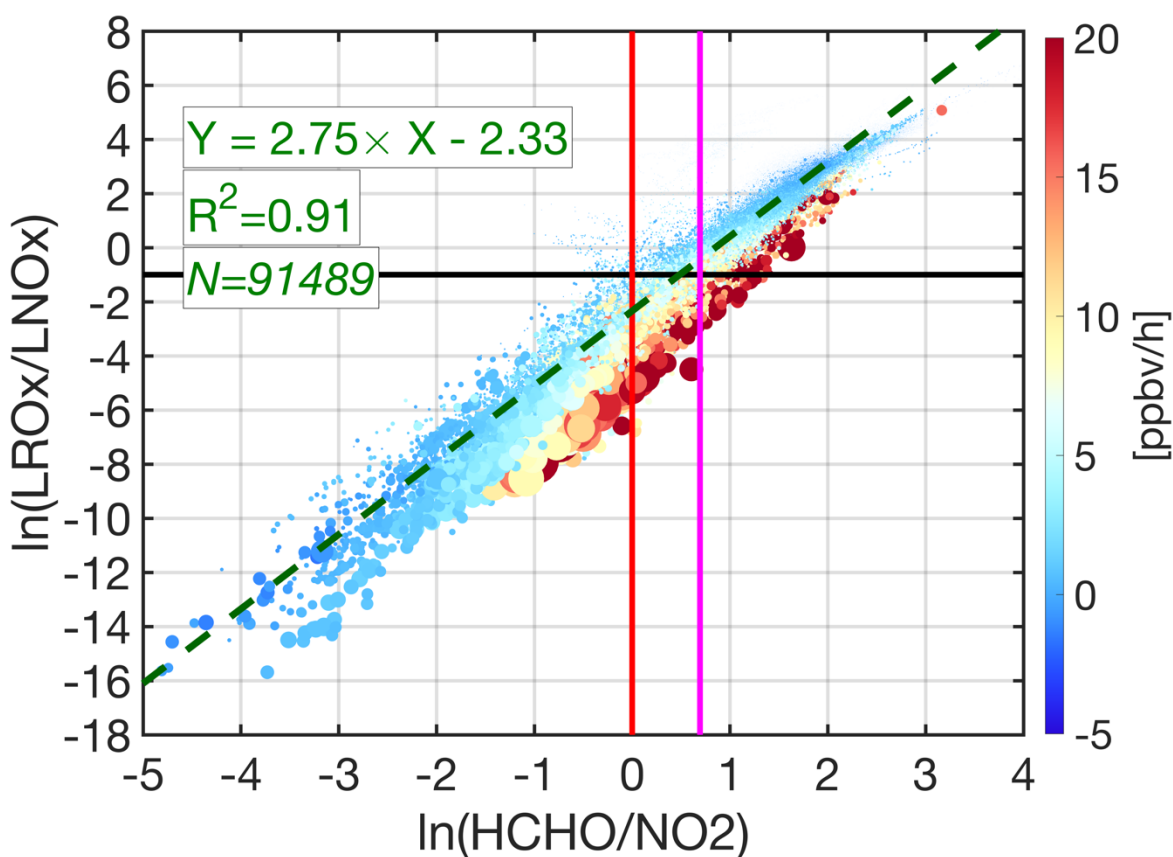
1269
 1270
 1271
 1272
 1273
 1274
 1275

Figure 1. The spatial distributions of aircraft measurements collected during NASA's a) DISCOVER-AQ Houston-Texas, b) DISCOVER-AQ Baltimore-Washington, c) DISCOVER-AQ Colorado, and d) KORUS-AQ. The duration of each campaign is based on how long the aircraft was in the air.



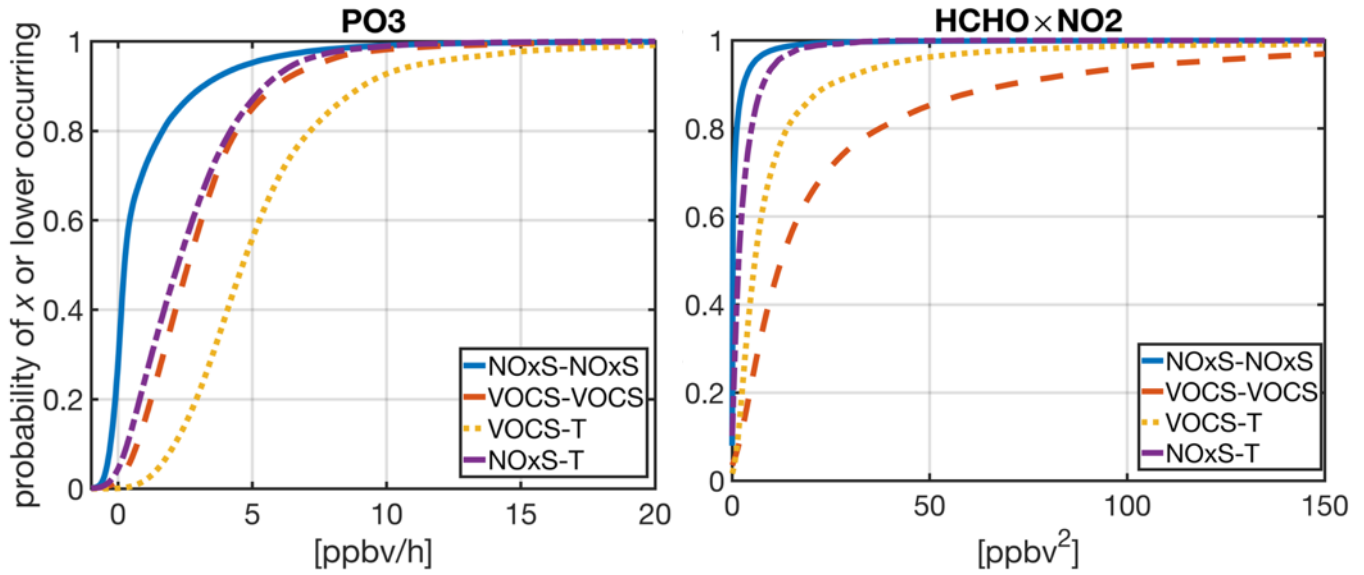
1276
1277

1278 **Figure 2.** The comparisons of the observed concentrations of several critical compounds to those
 1279 simulated by our FOAM box model. Each subplot contains mean bias (MB), mean absolute bias
 1280 (MAB), and root mean square error (RMSE). The least-squares fit to the paired data, along with
 1281 the coefficient of determination (R^2) are also individually shown for each compound. Note that we
 1282 do not account for the observations errors in the x-axis. The concentrations of NO and NO₂ are
 1283 log-transformed.

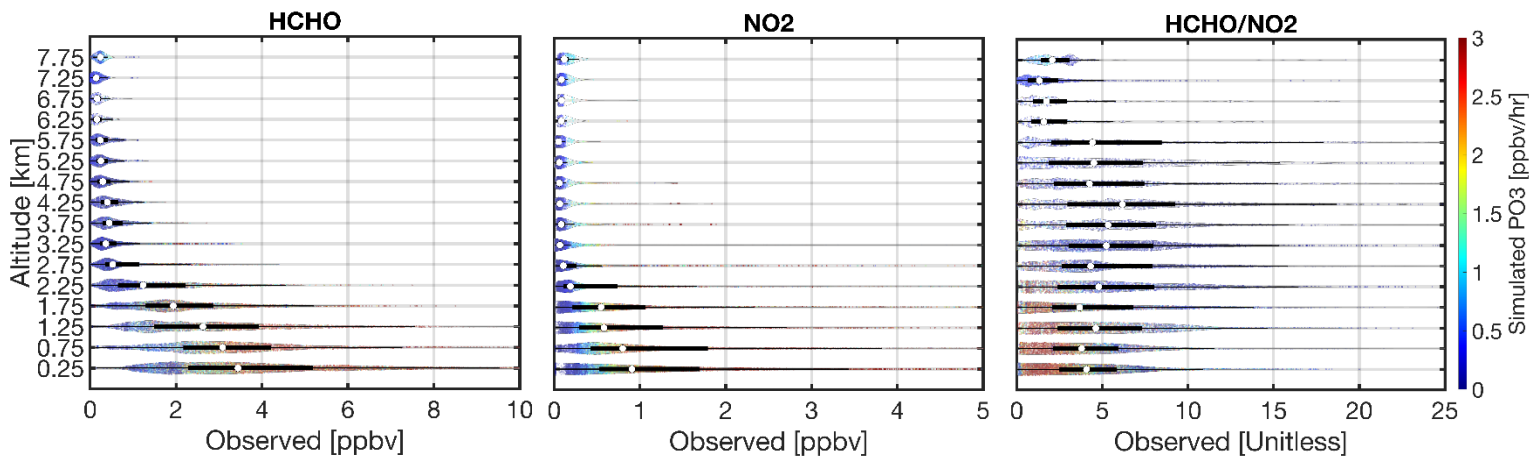


1284
 1285
 1286
 1287
 1288
 1289
 1290
 1291
 1292
 1293

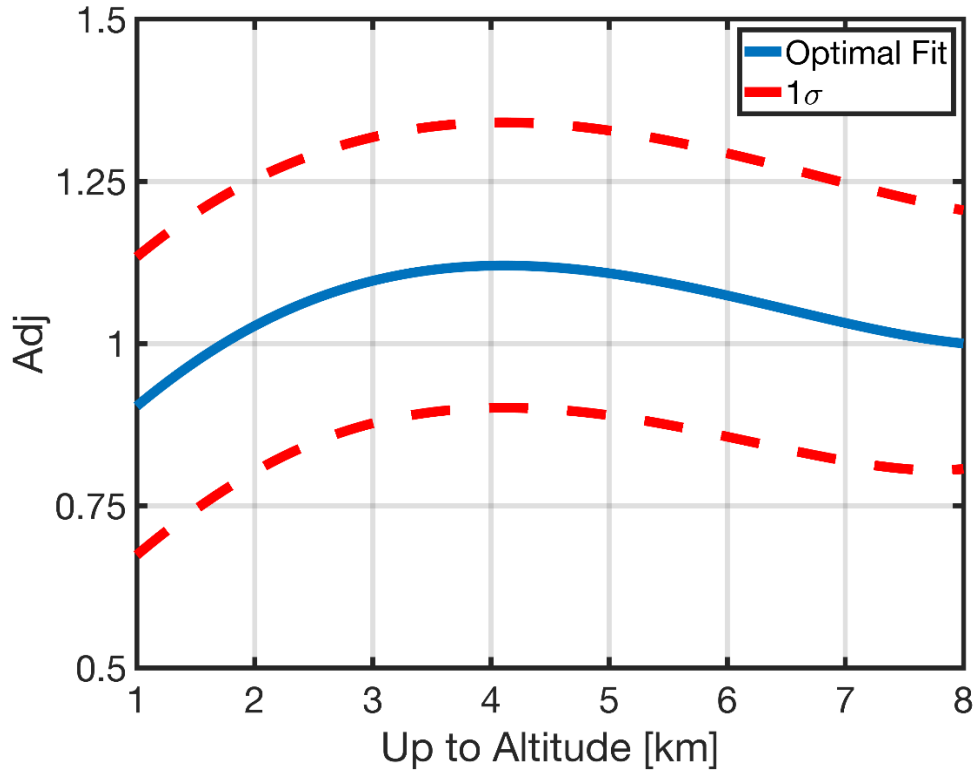
Figure 3. The scatterplot of natural logarithm-transformed of HCHO/NO₂ versus LROx/LNOx based on the simulated values performed by the F0AM box model. The heat color indicates the calculated ozone production rates (PO₃). The size of each data point is proportional to HCHO×NO₂. The black line is the baseline separator of NOx-sensitive (above the line) and VOC-sensitive (below the line) regimes. We overlay HCHO/NO₂=1 and HCHO/NO₂=2 as red and purple lines, respectively. The dashed dark green line indicates the least-squares fit to the paired data. The HCHO/NO₂ = 1.8 with a 20% error is the optimal transitioning point based on this result.



129
 1295 **Figure 4.** Cumulative distribution functions of PO_3 and $\text{HCHO} \times \text{NO}_2$ simulated by the box model
 1296 constrained by NASA's aircraft observations. Four regions are shown: NO_x -sensitive — NO_x -sensitive,
 1297 NO_x -sensitive—transitional, VOC-sensitive—transitional, and VOC-sensitive—VOC-sensitive. The first
 1298 name of the regime is based on the baseline ($\ln(\text{LRO}_x/\text{LNO}_x)=-1.0$), whereas the second one follows those
 1299 defined in Duncan et al. (2010): VOC-sensitive if $\text{HCHO}/\text{NO}_2 < 1$, transitional if $1 < \text{HCHO}/\text{NO}_2 < 2$, and
 1300 NO_x -sensitive if $\text{HCHO}/\text{NO}_2 > 2$.
 1301

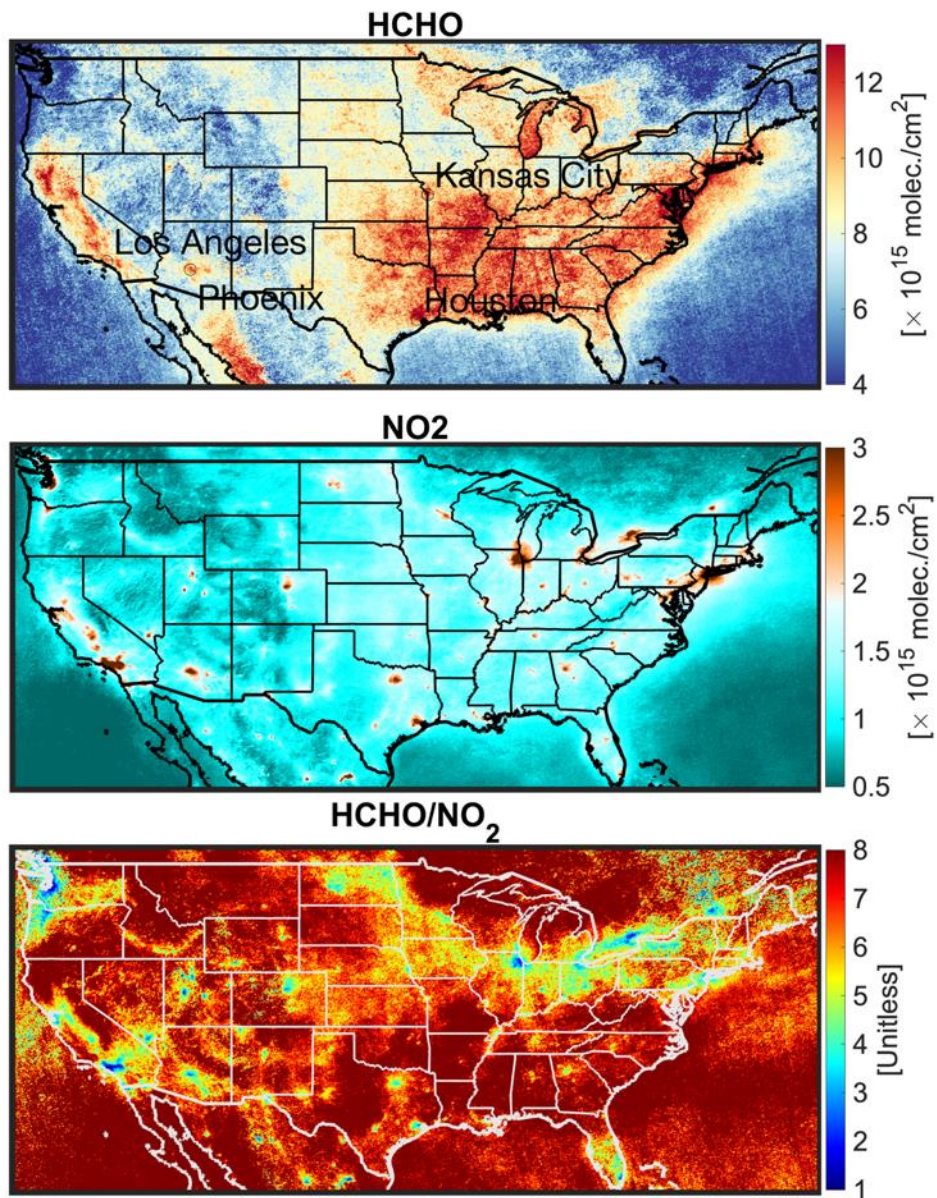


1303 **Figure 5.** The violin plots of the afternoon vertical distribution of HCHO, NO₂, and HCHO/NO₂
 1304 observations collected during DISCOVER-AQ Texas, Colorado, Maryland, and KORUS-AQ campaigns.
 1305 The violin plots demonstrate the distribution of data (i.e., a wider width means a higher frequency). White
 1306 dots show the median. A solid black line shows both the 25th and 75th percentiles. The heatmap denotes
 1307 the simulated ozone production rates.
 1308

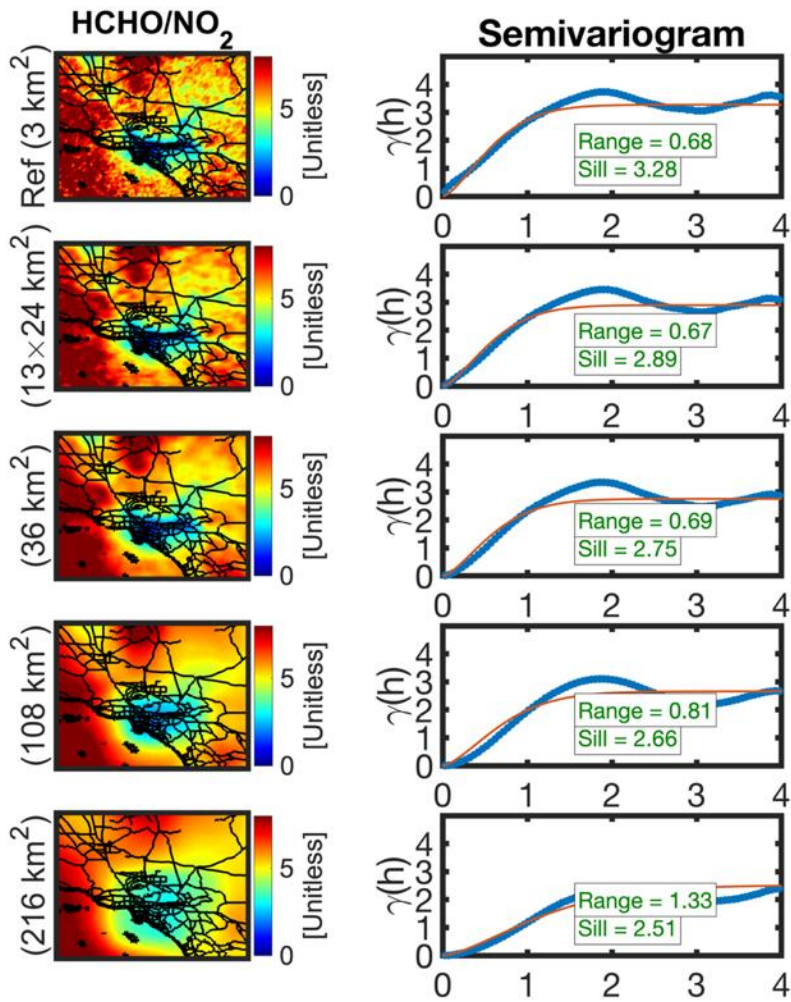


1309
 1310
 1311
 1312
 1313
 1314
 1315
 1316

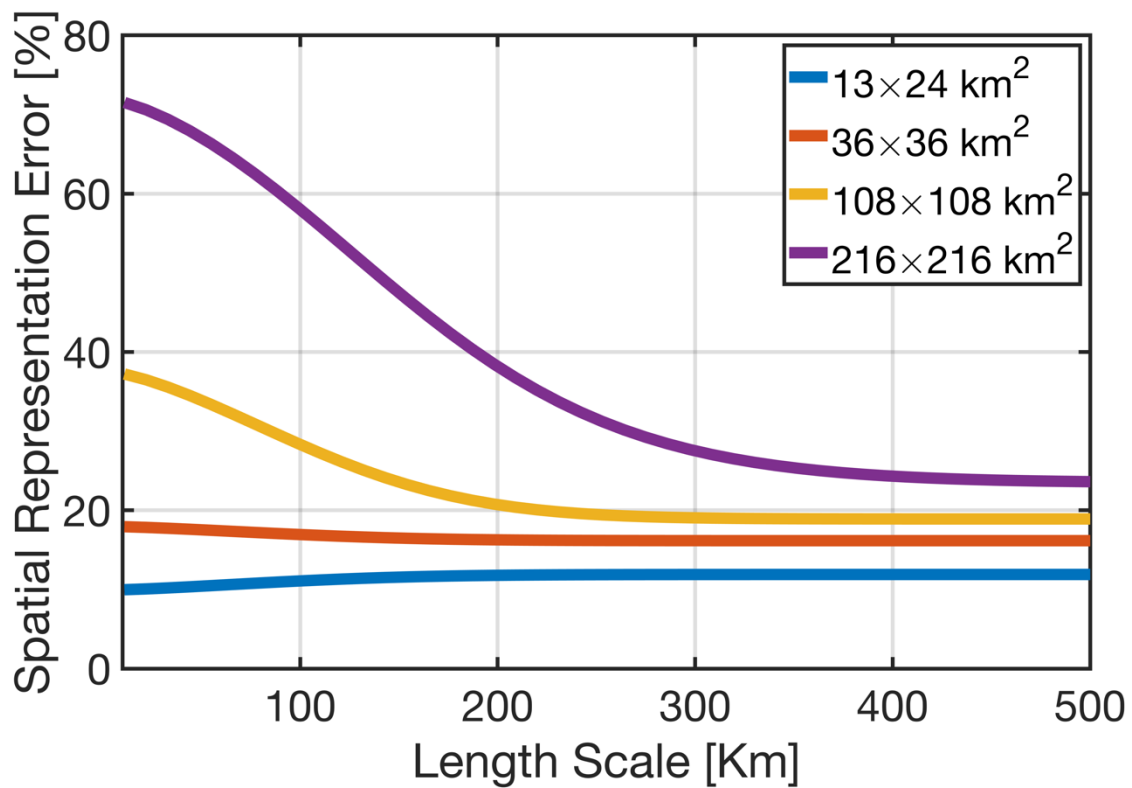
Figure 6. The adjustment factor is the ratio of the centroid of the polygon bounding 25th and 75th percentiles of the observed HCHO/NO₂ columns by NASA’s aircraft between the surface to 8 km to the ones between the surface and the desired altitude. This factor can be easily applied to the observed HCHO/NO₂ columns to translate the value to the desired altitude stretching down to the surface (i.e., PBLH). The optimal curve follows a quadratic function formulated in Eq.11.



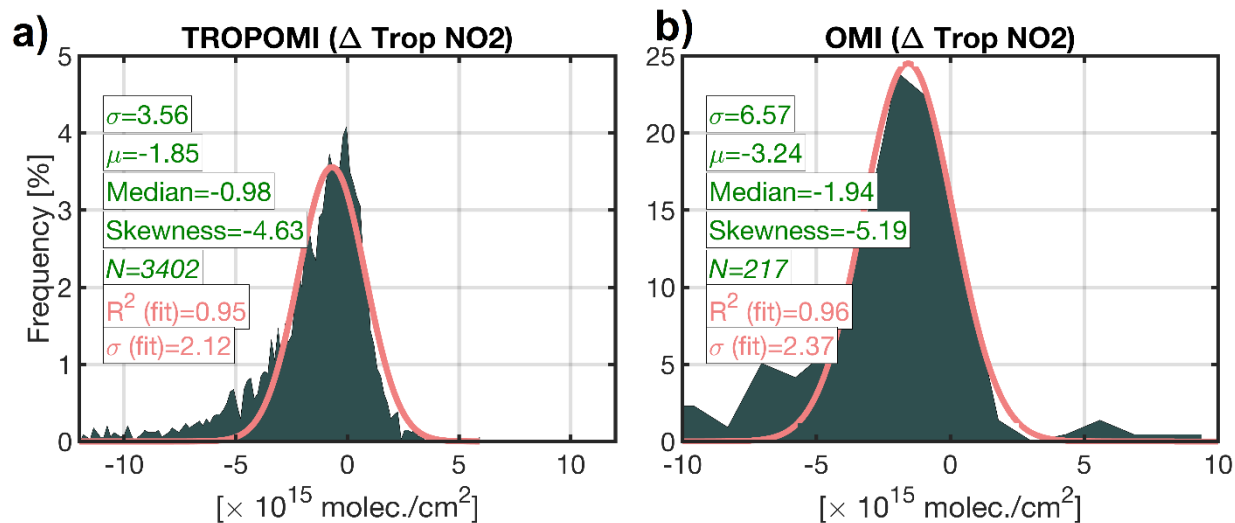
1317
 1318 **Figure 7.** Oversampled TROPOMI total HCHO columns (top), tropospheric NO₂ columns
 1319 (middle), and the ratio (bottom) at 3×3 km² from June till August 2021 over the US. The ratio map
 1320 is derived from the averaged maps shown in the top and middle panels.
 1321



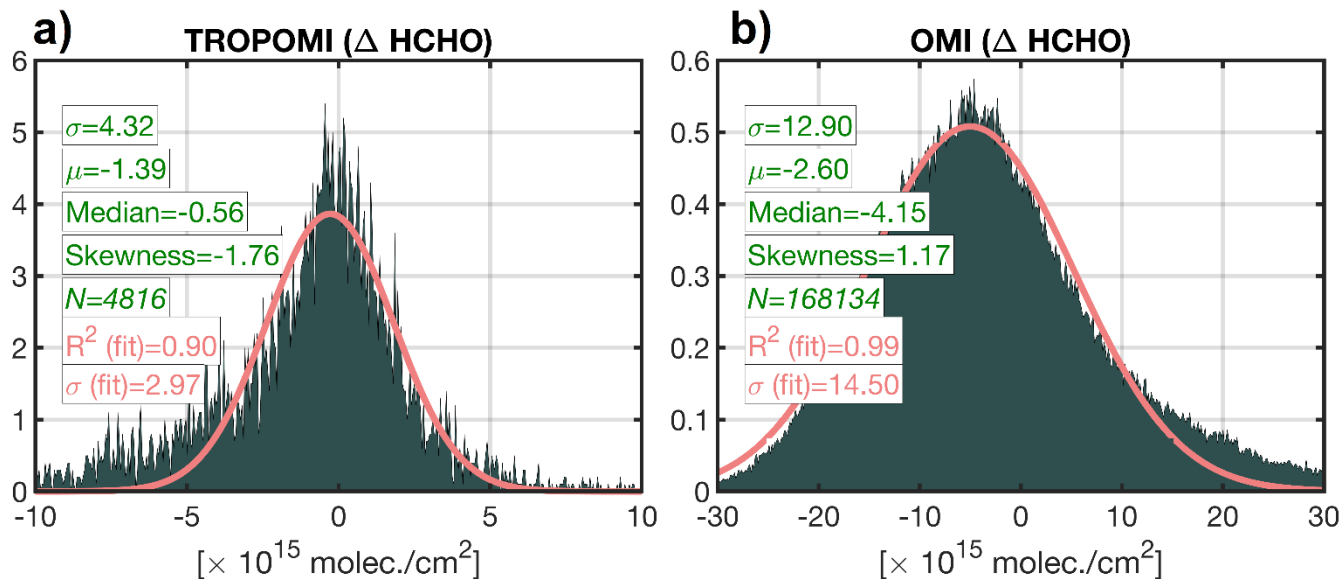
1322
 1323 **Figure 8.** The first column represents the spatial map of HCHO/NO₂ ratios over Los Angeles from
 1324 June till August 2021 at different spatial resolutions. To upscale each map to a coarser footprint,
 1325 we use an ideal box filter tailored to the target resolution. The second column shows the
 1326 semivariograms corresponding to the left map along with the fitted curve (red line). The sill and the
 1327 range are computed based on the fitted curve. The x-axis in the semivariogram is in degrees (1
 1328 degree ~ 110 km).
 1329



1330 **Figure 9.** The spatial representation errors quantified based on the proposed method in this study.
 1331 The error explains the spatial loss (or variance) due to the footprint of a hypothetical sensor at
 1332 different length scales. To put this error in perspective, a grid box with 216×216 km² will naturally
 1333 lose 65% of the spatial variance existing in the ratio at the scale of Los Angeles, which is roughly
 1334 50 km wide. All of these numbers are in reference to the TROPOMI 3×3 km².
 1335
 1336

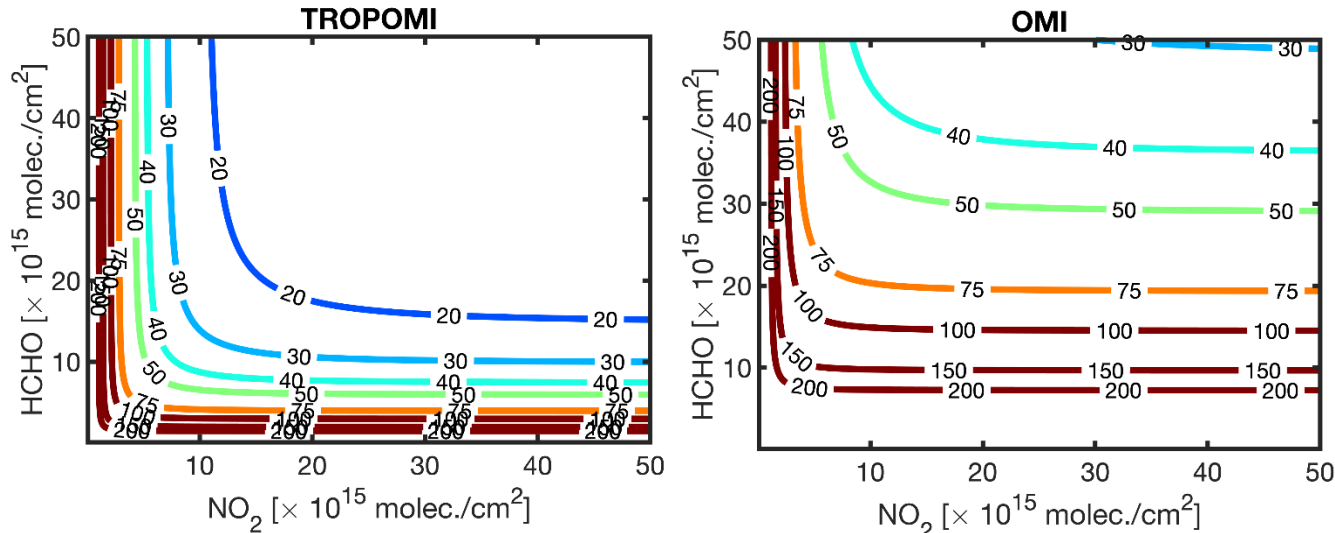


1337
 1338 **Figure 10.** The histogram of the differences between TROPOMI and OMI and benchmarks. MAX-
 1339 DOAS and integrated aircraft spirals are the TROPOMI and the OMI benchmarks, respectively.
 1340 The data curation and relevant criteria on how they have been paired can be found in Verholest et
 1341 al. (2021) and Choi et al. (2020). The statistics in green are based on all data, whereas those in
 1342 pink are based on the fitted Gaussian function.
 1343



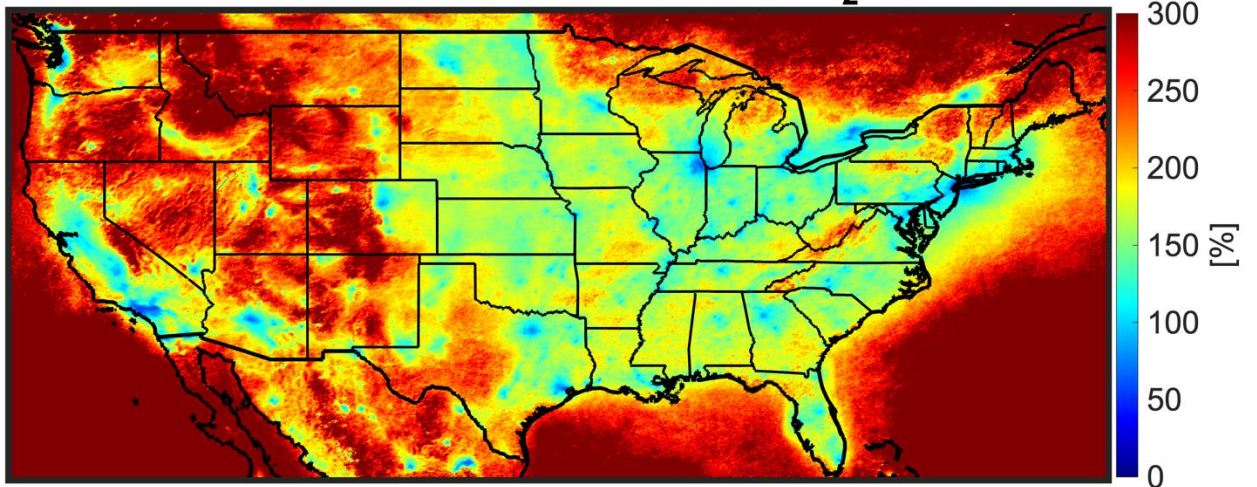
13
 1345 **Figure 11.** The histogram of the differences between TROPOMI and OMI and benchmarks. FTIR
 1346 and corrected GEOS-Chem simulations are the TROPOMI and the OMI benchmarks. The data
 1347 curation and relevant criteria on how they have been paired can be found in Vigouroux et al. (2021)
 1348 and Zhu et al. (2020). The statistics in green color are based on all data, whereas those in pink are
 1349 based on the fitted Gaussian function.

1350
 1351

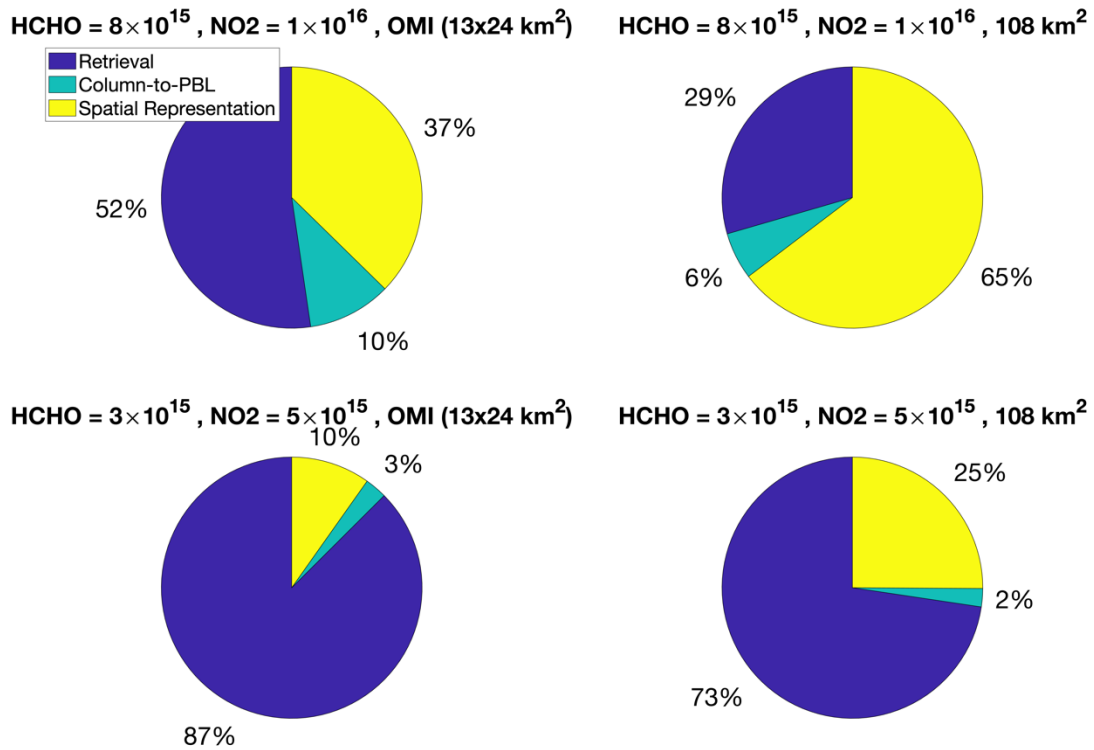


134
 1353 **Figure 12.** The contour plots of the relative errors in TROPOMI (left) and OMI (right) based on
 1354 dispersions derived from Figures 10 and 11. The errors used for these estimates are based on daily
 1355 observations.
 1356

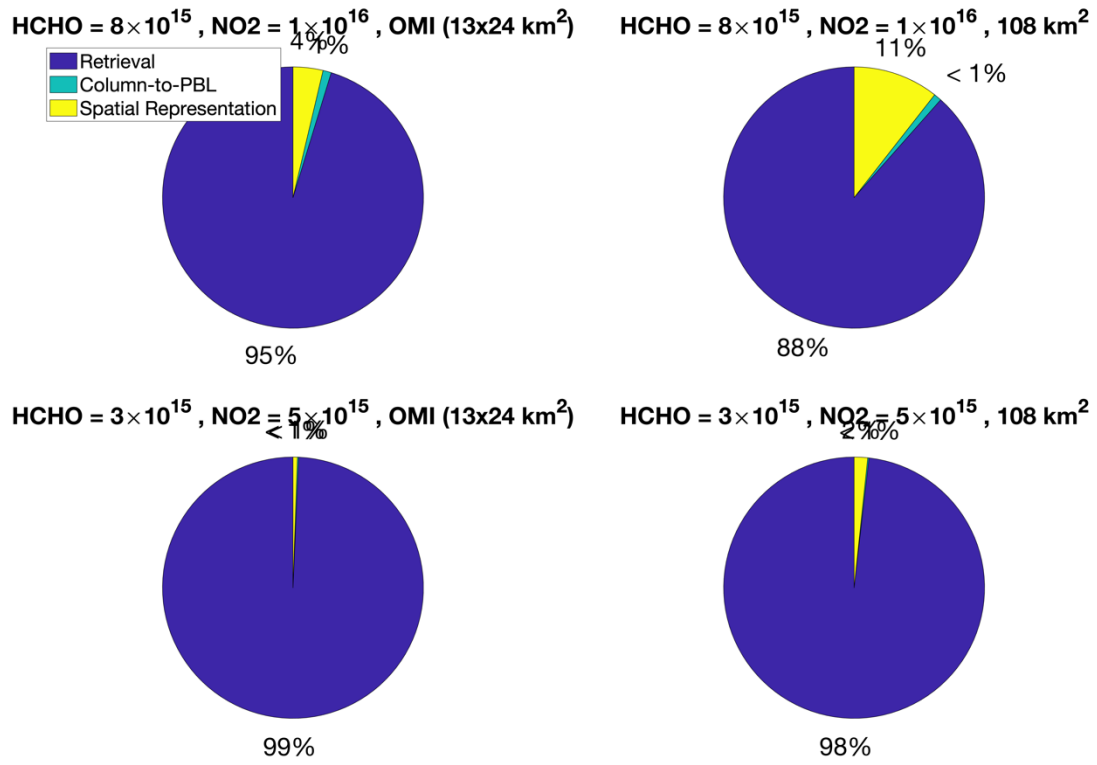
Total Relative Error in HCHO/NO₂



1357
1358 **Figure 13.** The total relative error for observed TROPOMI HCHO/NO₂ ratios considering the
1359 daily TROPOMI retrieval errors ($\sigma_{NO_2} = 2.11 \times 10^{15}$ molec./cm² and $\sigma_{HCHO} = 2.97 \times 10^{15}$
1360 molec./cm²), the spatial representation pertaining to OMI footprint over a city environment (13%
1361 loss in the spatial variance), and the column to the PBL translation parameterization (19%)
1362 proposed in this study. Please note that the observed FNR is based on mean values from June to
1363 August 2021, while the uncertainties used for error calculation are on a daily-basis.
1364
1365



1366
 1367 **Figure 14.** The fractional errors of retrieval (blue), column to PBL translation (green), and spatial
 1368 representation (yellow) of the total error budget for different concentrations and footprints based
 1369 on TROPOMI sigma values. The retrieval error used for the error budget is on a daily basis.



1370
1371
1372

Figure 15. Same as Figure 14 but based on OMI sigma values.